J. Fluid Mech. (2024), *vol*. 1000, A23, doi:10.1017/jfm.2024.1028

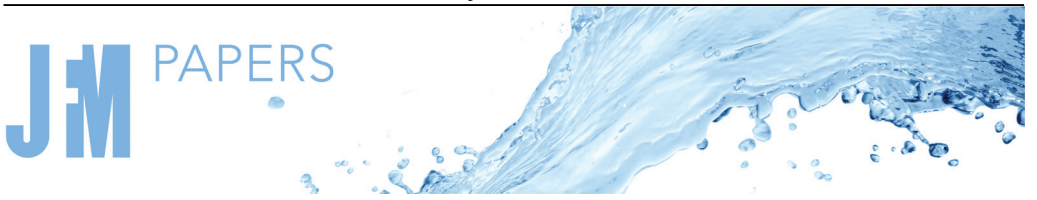

Experimental study on the effect of wall proximity on the flow around a cylinder under an axial magnetic field

Ze-Dong Wang[1], Qi-Long Zhang[1], Yuri B. Kolesnikov[2], Ze Lyu[1], Juan-Cheng Yang[3], Ming-Jiu Ni[1] and Nian-Mei Zhang[1],†

[1]School of Engineering Science, University of Chinese Academy of Sciences, Beijing 101408, PR China

[2]Technische Universitat Ilmenau, PF 100565, 98684 Ilmenau, Germany

[3]State Key Laboratory for Strength and Vibration of Mechanical Structures, School of Aerospace, Xi'an Jiaotong University, Xi'an 710049, PR China

(Received 30 July 2024; revised 24 October 2024; accepted 24 October 2024)

Investigations are conducted on the effect of wall proximity on the flow around a cylinder under an axial magnetic field, using the electrical potential probe technology to measure the velocity of liquid metal flow. The study focused on the impact of the inlet velocity of the fluid, the magnetic field and wall proximity on the characteristics of velocity fields, particularly on the vortex-shedding mode. Based on different magnitudes of the magnetic field and the distance from the cylinder to the duct wall, three types of vortex-shedding modes are identified, (I) shear layer oscillation state, (II) quasi-two-dimensional vortex-shedding states and (III) transition of the magnetohydrodynamic to hydrodynamic Kármán street. The transitions between these modes are analysed in detail. The experimental results show that the weak wall-proximity effect leads to the formation of the Kármán vortex street, while a reverse Kármán vortex street and secondary vortices emerge under a strong wall-proximity effect. It is noticed that the Kelvin–Helmholtz instability drives vortex shedding under regime I, leading to an increase in the Strouhal number (St) with stronger magnetic fields. Additionally, under a strong axial magnetic field, the wall-proximity effect ('Shercliff layer effect') promotes the instability of shear layers on both sides of the cylinder. These unique coupling effects are validated by variations in modal coefficients and energy proportions under different vortex-shedding regimes using the proper orthogonal decomposition method.

Key words: vortex shedding, vortex dynamics

† Email address for correspondence: nmzhang@ucas.ac.cn

1. Introduction

Nuclear fusion is a good selection for energy production in the future due to its several potential advantages including high energy density, no greenhouse gas emissions and so on. While these advantages are compelling, significant scientific and engineering challenges have yet to be solved, which impede the economical production of fusion energy. The International Thermonuclear Experimental Reactor (ITER) has been designed to demonstrate the feasibility of nuclear fusion. Among the components in a fusion reactor such as the tokamak reactor, a kind of liquid metal blanket is selected due to the advantages of heat transfer and tritium breeding capabilities (Abdou *et al.* 2015). However, the existence of strong magnetic fields and high temperature gradients introduces challenges such as Lorentz and buoyancy forces, which must be carefully managed in the design of the liquid metal blanket to ensure high efficiency in heat and mass transfer (Smolentsev *et al.* 2015; Mistrangelo *et al.* 2021; Smolentsev 2023). Until now, previous studies have proved that the adoption of vortex generators such as ribs, fins, grooved surfaces and obstacles in the flow channel can improve the heat transfer efficiency (Cassells, Hussam & Sheard 2016; Hussam *et al.* 2018; Kusumi *et al.* 2019). A circular cylinder in proximity to a wall, as a traditional method of vortex promotion, generates quasi-two-dimensional (Q2-D) vortices under the magnetic field, effectively improving convection heat transfer (Moreau 1990; Husssam, Thompson & Sheard 2011; Hussam & Sheard 2013). Studying the dynamic characteristics of magnetohydrodynamics (MHD) flow around an obstacle is highly beneficial for understanding heat transfer enhancement mechanisms.

The Lorentz force, induced by the liquid metal flow through a magnetic field, alters the dynamic characteristics of the Kármán vortex street. A strong magnetic field introduces a Q2-D flow state, as outlined in the Sommeria & Moreau (1982) 'SM82 model'. This model suggests that perturbations along the magnetic field such as turbulence and vortices, exhibit strong anisotropy due to the Lorentz force. The MHD flow around a cylinder under an axial magnetic field has been extensively researched in recent decades (e.g. Andreev & Kolesnikov 1998; Mück *et al.* 2000; Frank, Barleon & Müller 2001; Dousset & Pothérat 2008; Dousset & Pothérat 2012; Kanaris *et al.* 2013; Rhoads, Edlund & Ji 2014; Chatterjee & Gupta 2015; Hamid *et al.* 2015). The presence of an axial magnetic field serves to delay the onset of flow separation and vortex shedding, thereby contributing to a markedly increased critical Reynolds number (Re_{cr}) compared with that observed in hydrodynamic flows. As a result, Re_{cr} for vortex shedding in MHD flow maintains a linear relationship with the Hartmann number (Ha) ($Re_{cr}/Ha \approx 0.47$, see Frank *et al.* 2001), quantifying the magnetic field strength. Moreover, Mück *et al.* (2000) pointed out that the Kármán vortex street transitions from three-dimensional to Q2-D columnar vortices (also illustrated in Davidson 1997; Müller & Bühler 2001) when the interaction parameter N is greater than 1. Rhoads *et al.* (2014) experimentally observed Kármán vortex street using electrical potential probes for $0 < N < 2$.

Concerning the fluid around a circular cylinder near a wall, a substantial body of research has been conducted in the field of hydrodynamics. The findings indicate that the wall-proximity effect exerts a direct influence on the vortex dynamics characteristics and the flow transition after an obstacle (e.g. Bearman & Zdravkovich 1978; Kiya, Tamura & Arie 1980; Zdravkovich 1997; Zovatto & Pedrizzetti 2001; Dipankar & Sengupta 2005; He *et al.* 2017; Jiang & Cheng 2017; Thompson *et al.* 2021; Zhou *et al.* 2021). It involves complex interactions among three shear layers: a boundary layer, a separating free shear layer and a wake street (Williamson 1996). The wall-proximity effect leads to separation delay, transitioning the wake region from unsteady to steady (see Bearman & Zdravkovich 1978; Zovatto & Pedrizzetti 2001). The aforementioned delayed separation

indicates that the wall-proximity effect suppresses the instability observed in the wake street. Additionally, He *et al.* (2017) noted that secondary vortex shedding from the wall shear layer, induced by an inverse pressure gradient, pushes the vortex street away from the wall. These secondary vortices significantly influence the wake trajectory and vortex intensity, leading to asymmetric velocity fluctuations.

However, to the authors' knowledge, studies on MHD flow around a cylinder with the wall-proximity effect are rare, with only some Q2-D numerical studies focusing on heat transfer (Hussam *et al.* 2011; Hussam & Sheard 2013). The three-dimensional effects, such as the Shercliff layer effect and the additional Joule dissipation caused by three-dimensional effects, have often been neglected in Q2-D simulations (e.g. Dousset & Pothérat 2008) and in some experiments (e.g. Belyaev *et al.* 2022), which, however, exhibit a significant effect on vortex shedding in this work. The three-dimensional (3-D) effects on the duct flow have been discussed in previous research by 3-D simulation (Mück *et al.* 2000; Pothérat 2007; Cassells *et al.* 2019). An experimental study is necessary to examine the strong 3-D effect, especially the wall-proximity effect on the MHD vortex street, which is the main purpose of the present study.

Several numerical studies for MHD flow around a cylinder with the wall-proximity effect have been conducted to enhance heat transfer (Hussam *et al.* 2011; Hussam & Sheard 2013). Using Q2-D models, these studies focused on the influence of the blockage ratio and the gap ratio (G/d, defined as the ratio of the distance G from the bottom edge of the cylinder to the cylinder's diameter d) on heat transfer rather than the MHD effect. Hussam & Sheard (2013) noted that large blockage ratio (β, defined as the ratio of the cylinder's diameter d to the channel height H) improves heat transfer but at a great cost of pressure drop. In addition, a small blockage ratio ($\beta = 0.1$) with the effect of placing a circular cylinder close to the wall ($G/d \approx 1$) optimizes heat transfer with a small pressure drop in a Q2-D simulation, leading to high energy efficiency. Hussam *et al.* (2011) investigated the impact of the wall-proximity effect on heat transfer, with insufficient analysis of the vortex-shedding regime. In addition, the combined influence of the magnetic field and the gap ratio on the vortex-shedding regimes requires further detailed examination. Therefore, this study explores how the wall-proximity effect (G/d) influences the vortex shedding under various magnetic fields.

Furthermore, there is a lack of exploration into the variation of the Strouhal number (St) and the understanding of the flow regime under MHD conditions. Kolesnikov & Tsinober (1976) and Andreev & Kolesnikov (1998) observed an increase in shedding frequency with an increase of Ha in their experiments. Moreover, they found that minor velocity fluctuations were observed within the shear layer of the cylinder, while significant velocity fluctuations were observed $1.5d$ downstream of the cylinder using electrical potential probes. They attributed this phenomenon to the oscillations of the shear layers stretched by the magnetic field at the rear of the cylinder. The numerical simulation in Hussam, Thompson & Sheard (2012) with a small disturbance in the incoming flow confirmed this phenomenon.

The phenomenon of St increasing with the augmentation of the magnetic field was also observed in other research. Mück *et al.* (2000) attributed the increase in the shedding frequency to the augmentation of the magnetic field to a square cylinder rather than a circular one. Dousset & Pothérat (2008) and Hussam *et al.* (2011) provided the evolution of St against Re for different Hartmann numbers (Ha). At a value of Re of approximately 3800, there was a decrease in the shedding frequency followed by an increase with the strengthening of the magnetic field. However, the authors did not offer any further discussion. Chatterjee & Gupta (2015) also observed the trend of St increasing with Ha,

attributing this to the secondary vortices generated by the instability of the wall boundary layer. Nevertheless, previous researchers have been unable to reach a consensus on the mechanism by which the saturation parameter increases with the strength of the magnetic field.

In light of the latest research findings, previous researchers have identified different flow regimes under varying magnetic field conditions, except for a stable state when the Hartmann number (*Ha)* is sufficiently high or the Reynolds number (*Re*) is too low. Mück *et al.* (2000) identified two flow regimes with $\beta = 0.1$: one dominated by inertial forces under a weak magnetic field, similar to the Kármán vortex street in hydrodynamics, and another dominated by Lorentz forces under a strong magnetic field, where the vortex street becomes Q2-D columnar vortices due to Hartmann friction (Frank *et al.* 2001; Hussam *et al.* 2011). Dousset & Pothérat (2008) using the SM82 model obtained two vortex-shedding regimes (Chatterjee & Gupta 2015): one with only vortex streets and another with interactions between vortex streets and secondary vortices, shedding from the Shercliff layers because of Kelvin–Helmholtz (K-H) instability (with $\beta = 0.25$). In this study, the results indicate that there are three distinct unsteady stages in the trend of *St* against the Hartmann friction parameter (*Ha*/*Re*), which suggests that there is still insufficient understanding of the variation of *St* and the flow regimes under MHD conditions. Furthermore, it is essential to investigate the impact of wall proximity on the vortex street under varying *Re* and *Ha* conditions. The objective of this study is twofold: firstly, to elucidate the mechanism behind the increase in shedding frequency with the strengthening magnetic field; and secondly, to investigate the wall-proximity effect on vortex dynamic characteristics.

The remainder of this paper is organized as follows: § 2 presents the Navier–Stokes equation for the MHD effect and the SM82 model. Section 3 details the experimental arrangement, measurement methods and verifications. Section 4 provides a detailed discussion of the main results. Section 5 summarizes the conclusions.

2. Basic equations with Lorentz force effect

2.1. *Three-dimensional Navier–Stokes equations for MHD*

The magnetic Reynolds number (Re_m), which characterizes the relative effects of induction of a magnetic field to the magnetic diffusion, is defined as $Re_m = \mu\sigma U_0 a$, where μ represents the magnetic permeability, σ denotes the electrical conductivity, U_0 stands for the mean flow velocity and a is the channel width. The values of these parameters are provided in table 1. The value of $Re_m \sim O(10^{-3})$ in this work is significantly less than 1, so the induced magnetic field is negligible but not the induced currents (Pan, Zhang & Ni 2019; Zhang *et al.* 2023). The conservation of mass, non-dimensional momentum, charge and Ohm's law for incompressible and conductive fluids like liquid metals are, respectively,

$$\nabla \cdot \boldsymbol{u} = 0, \tag{2.1}$$

$$\frac{\partial \boldsymbol{u}}{\partial t} + (\boldsymbol{u} \cdot \nabla)\boldsymbol{u} = -\nabla p + \frac{1}{Re}\Delta \boldsymbol{u} + N(\boldsymbol{j} \times \boldsymbol{B}), \tag{2.2}$$

$$\nabla \cdot \boldsymbol{j} = 0, \tag{2.3}$$

$$\boldsymbol{j} = -\nabla \Phi + \boldsymbol{u} \times \boldsymbol{B}, \tag{2.4}$$

where p denotes the pressure, ρ the fluid mass density, $\boldsymbol{B}$ the magnetic field, $\boldsymbol{u}$ the velocity vector, Φ the electrical potential and v its kinematic viscosity. The term $N(\boldsymbol{j} \times \boldsymbol{B})$

Parameters	Quantity	Values
Diameter of cylinder	d, mm	6
Width of cross-section	a, mm	40
Height of cross-section	$H = 2b$, mm	60
Average velocity U_0	U_0, m s^{-1}	0.0090–0.0404
Density of Galinstan	ρ, kg m^{-3}	6360
Magnetic Permeability	μ, H m^{-1}	$\sim 1.0 \times 10^{-6}$
Conductivity of Galinstan	σ, $\Omega^{-1}\cdot$m^{-1}	3.10×10^{6}
Kinematic viscosity of Galinstan	ν, m^2 s^{-1}	2.98×10^{-7}
Magnetic field strength	B, T	0.05–1.0
Blockage ratio	$\alpha = d/H$	0.1
Gap ratio	G/d	0.5, 1.0, 1.5, 2.0, 2.5, 3.0
Reynolds number Re_d (Re)	$Re_d = U_0 d/\nu$	180–810
Reynolds number Re_{ch}	$Re_{ch} = U_0 a/\nu$	1200–5400
Hartmann number Ha_d	$Ha_d = Bd(\sigma/\rho\nu)^{0.5}$	12.1–242.4
Hartmann number Ha_{ch} (Ha)	$Ha_{ch} = Ba(\sigma/\rho\nu)^{0.5}$	81–1616
Interaction parameter N	$N = Ha_{ch}^2/Re_{ch}$	$1.2–2.2 \times 10^{3}$
Frequency of vortex shedding f	f	—
Strouhal number St	$St = fd/U_0$	—

Table 1. Physical and non-dimensional parameters in the experiments.

represents the Lorentz force. The ratio of electromagnetic forces and viscous forces can be expressed as the interaction parameter N (where $N = Ha^2/Re$). The interaction between the induced currents and the magnetic field generates Lorentz forces that tend to damp velocity variations along the streamlines (Sommeria & Moreau 1982).

2.2. *The SM82 model under a strong magnetic field*

In MHD channel flow with insulated walls, the boundary layer perpendicular to the direction of the magnetic field is called the Hartmann layer (the Hartmann layer's thickness $\delta_H \sim Ha^{-1}$), while the boundary layer parallel to the direction of the magnetic field is referred to as the Shercliff layer (the Shercliff layer's thickness $\delta_S \sim Ha^{-0.5}$, Hunt & Ludford 1968). When the magnetic field is sufficiently strong, the induced currents pass entirely through the boundary layers. Meanwhile, the velocity gradient in the core region along the direction of the magnetic field equals zero, while the velocity gradient only exists in the boundary layers. Therefore, the flow in the core region is two-dimensional, and referred to as Q2-D flow (Moreau 1990). As the velocity gradient along the direction of the magnetic field approaches zero ($\partial u/\partial y = 0$), (2.1) and (2.2) through (2.4) can be simplified to the following form:

$$\nabla \cdot \boldsymbol{u}_\perp = 0, \tag{2.5}$$

$$\frac{\partial \boldsymbol{u}_\perp}{\partial t} = -(\boldsymbol{u}_\perp \cdot \nabla_\perp)\boldsymbol{u}_\perp - \nabla_\perp p_\perp + \frac{1}{Re}\nabla_\perp^2 \boldsymbol{u}_\perp - 2\frac{d^2}{a^2}\frac{Ha}{Re}\boldsymbol{u}_\perp. \tag{2.6}$$

By taking d, ρU_0^2 and d/U_0 as the typical length, pressure and time, respectively, the Lorentz force is simplified to a linear friction term, as shown in (2.5) and (2.6). The linear Hartmann friction parameter (Ha/Re) is also called the Hartmann damping term, a dominant parameter for vortex shedding under a magnetic field. In addition, the linear friction parameter Ha/Re caused by the Hartmann layer is considered as the effective ratio

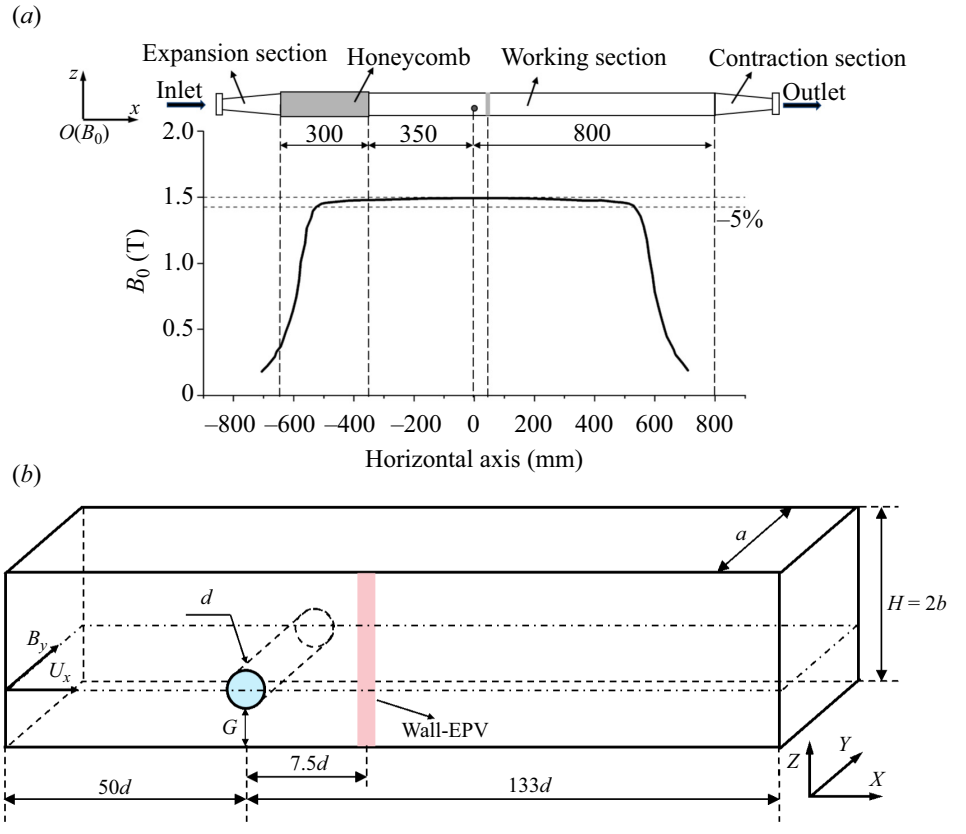

Figure 1. (*a*) Configuration of the test section and the *x*-distribution component of the imposed magnetic field B_0. (*b*) Schematic diagram of the experimental set-up.

of Lorentz forces to inertial forces (see Sreenivasan & Alboussière 2002; Chatterjee & Gupta 2015).

The fundamental principle behind using electrical potential probes to measure velocity is based on Ohm's law $\boldsymbol{j} = \sigma(\boldsymbol{E} + \boldsymbol{u} \times \boldsymbol{B})$, where $\boldsymbol{E}$ denotes the electric field. This law relates the electric potential measured by the probes to the flow velocity, enabling the determination of fluid speed through the analysis of electrical properties within the flow field.

3. Experimental set-up and validation

3.1. *Configuration of the liquid metal loop*

Experiments were conducted using a liquid metal loop at the University of Chinese Academy of Sciences (UCAS), known as the Magneto-Thermo-Hydrodynamic (MaTHE) loop. The experiments were performed in an insulated channel (see figure 1*a*), oriented horizontally within a uniform magnetic field. The field was created by an electromagnet with overall pole dimensions of 1200 mm length and 320 mm height, in a gap of 80 mm. The electromagnet can generate a magnetic field (B_0) of up to 2.0 Tesla (T), with inhomogeneity maintained below 5 % to ensure uniformity. Fluid motion within the channel was driven by an electromagnetic pump (EMP60-GA), with fluctuations ranging from 4 % (when $Re = 180$) to 1 % (when $Re = 810$) during the experiments.

The metallic fluid flows through a pipeline into a heat exchanger, where the temperature is regulated to 22 ± 0.5 °C. Subsequently, it passes through an electromagnetic flowmeter (Emerson 8711 series), which upholds an accuracy class of 0.2 with a volumetric flow rate range from 0 to 0.8 $\mathrm{m^3\ h^{-1}}$. Finally, liquid metal fluid flows into the inlet of the test section.

To further refine the flow quality entering the measurement section, two 3D-printed honeycomb structures were incorporated upstream of the inlet. These honeycombs played a pivotal role in enhancing the uniformity of the flow entering the channel, effectively mitigating large-scale turbulence and flow inconsistencies at the entry cross-section. The upstream honeycomb was situated at the entry of the magnetic field to minimize the potential gradient effect, as supported by Belyaev *et al.* (2021). The liquid metal flowed through the contraction section, honeycomb section, fully developed section and finally flowed around a cylinder. The cylinder, with its axis parallel to the magnetic field and capable of modifying its distance from the bottom wall, was positioned more than 650 mm (exceeding $108d$) downstream from the flow inlet. This distance ensures the flow is fully developed before encountering the cylinder.

Additional aspects related to the experimental set-up, such as configuration details, measurement techniques and verification procedures, are elaborated in the following subsections of § 3.

3.2. *Parameters and variables in the experiments*

All the walls and the cylinder were made of acrylic to maintain insulated boundary conditions. The channel, with a width (a) of 40 mm and a half-height (b) of 30 mm (see figure 1*b*), yields a blockage ratio (β) of approximately 0.1 and an aspect ratio (α) of 6.67.

Galinstan, a eutectic alloy comprising gallium (Ga), indium (In) and tin (Sn) in the ratio of 67 %, 20.5 % and 12.5 % respectively, served as the working fluid. The physical properties of $Ga_{67}In_{20.5}Sn_{12.5}$, including density ($\rho$), kinematic viscosity ($\nu$) and electrical conductivity (σ) at an operational temperature of 22 ± 0.5 °C are listed in table 1 (refer to Morley *et al.* 2008).

The flow rate varied from 0.078 to 0.350 $\mathrm{m^3\ h^{-1}}$, achieving a mean velocity (U_0) ranging from 0.0090 to 0.0404 $\mathrm{m\ s^{-1}}$. These velocities correspond to Reynolds numbers (Re_d, also Re in this work) spanning from 180 to 810 based on the cylinder's diameter, and Reynolds numbers (Re_{ch}) ranging from 1200 to 5400 based on the channel height. The magnetic field was varied from 0.05 to 1.0 T, allowing exploration of Ha_d from approximately 12.1 to 242.4 and Ha_{ch} (also Ha in this work) from 81 to 1616. The experiments were conducted with six gap ratios G/d ranging from 0.5 to 3.0 to examine the wall-proximity effect. For each Reynolds number (Re_{ch}) and Hartmann number (Ha_{ch}), the interaction parameter (N) ranged from 1.2 to 2.2×10^3, all of which are greater than one, fulfilling the prerequisites of the SM82 model by Sommeria & Moreau (1982). This adherence confirms the Q2-D nature of the flow under the influence of the magnetic field. Other non-dimensional parameters, including the Strouhal number (St) and set-up characteristics, are also provided in table 1.

3.3. *Velocity measurements by electrical potential probes*

To accurately capture fluid flow under a magnetic field, wall electrical potential probes (Wall-EPV, see figure 1) were employed to measure velocity through potential differences (Eckert, Cramer & Gerbeth 2007). As depicted in figure 2, the probes, positioned at $x = 7.5d$ downstream from the cylinder, were inserted into specifically designated slots

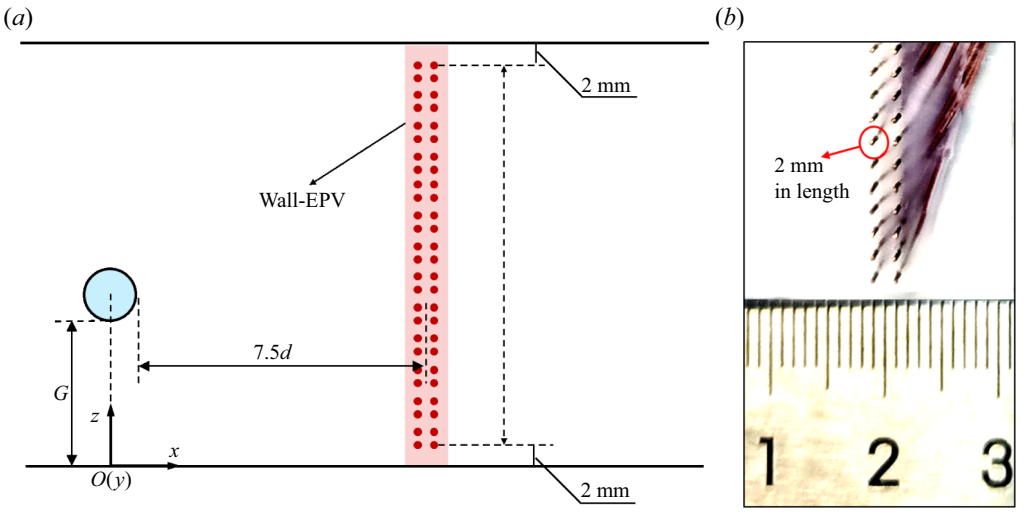

Figure 2. Arrangement and detailed configuration of the wall electrical potential probes. (*a*) Arrangement of the wall electrical potential probes and (*b*) photo of the electrical potential probes.

on one side of the channel wall. The placement, at 7.5d downstream from the cylinder, is a proper position for capturing the evolved flow patterns, such as the Kármán vortex street (Frank *et al.* 2001; Rhoads *et al.* 2014; Zhang *et al.* 2023).

In the presence of a sufficiently strong magnetic field, the core flow exhibits Q2-D characteristics (referred to as the SM82 model), maintaining nearly constant potential along the magnetic field direction (see Sommeria & Moreau 1982; Pothérat & Klein 2014). However, Mück *et al.* (2000) noted that the potential distribution is not strictly two-dimensional under a strong magnetic field. The potential isolines along the direction of the magnetic field exhibit a certain curvature. The potential differences measured by non-intrusive wall probes may fall below the measurement accuracy. In this case, non-intrusive potential probes can no longer detect existing cigar-like vortices (Mück *et al.* 2000). Therefore, the probes were immersed 2 mm into the fluid to measure the electrical potential difference of the core flow, thrusting across the thickness of the Shercliff layer (δ_S) (see Sommeria & Moreau 1982; Cassells *et al.* 2019). Simultaneously, this approach prevented the adhesion of oxides to the tip of probes and ensured the rigidity of the potential probes. The effectiveness of wall electrical probes has been verified by prior studies (e.g. Burr *et al.* 2000; Frank *et al.* 2001; Messadek & Moreau 2002; Sreenivasan & Alboussière 2002; Mistrangelo & Bühler 2018; Bühler, Mistrangelo & Brinkmann 2020).

During the experiments, a data acquisition system comprising 58 voltage channels was sampled simultaneously at a frequency of 250 Hz over a duration of 300 seconds. The sampling frequency was designed to cover the vortex-shedding frequency range of approximately 1.5 Hz, ensuring multiple shedding cycles were captured.

To eliminate potential noise, specifically the 50 Hz electrical noise, a low-pass filter with a 45 Hz cutoff was implemented. Subsequently, signal quality was refined by subtracting the average noise level, measured under identical magnetic conditions but in the absence of flow. The resultant signals, with a noise floor below 2 microvolts and signal strength exceeding 10 microvolts, yielded a signal-to-noise ratio exceeding 5, indicating high-quality measurements.

Following the principles outlined in the SM82 model, velocity measurements are derived from the potential differences recorded by the probes. Previous studies have examined errors stemming from the internal currents on the measured potential gradient,

suggesting negligible impact at $N \gg 1$ and $Ha \gg 1$ (see Frank *et al.* 2001; Messadek & Moreau 2002; Belyaev *et al.* 2022). During the experiments, the minimum Ha is 81 and the minimum N is 1.21, satisfying the assumptions proposed by the SM82 model. The formula for velocity calculation are as follows:

$$u(x, z) = \frac{\phi_{wall}(x, z + \Delta z) - \phi_{wall}(x, z)}{c_1 B_0 \Delta z}, \tag{3.1}$$

$$w(x, z) = -\frac{\phi_{wall}(x + \Delta x, z) - \phi_{wall}(x, z)}{c_1 B_0 \Delta x}, \tag{3.2}$$

where ϕ_{wall} is the electric potential difference of two adjacent probes. The distances between the two adjacent probes in the x-direction and z-direction are $\Delta x = 2$ mm and $\Delta z = 2$ mm, respectively. The coefficient c_1 depends on the condition of closing the induced currents. For Hartmann numbers greater than 200, c_1 approaches unity, aligning the probe-measured velocity with actual flow velocities (Belyaev *et al.* 2022). If Ha is not large enough, c_1 becomes greater than unity, resulting in a larger velocity than its actual value.

To illustrate the impact of upstream probes on downstream probes, the probe can be considered as cylinders with a diameter of 0.35 mm. The calculated Reynolds number (Re_{probe}) ranges from 10.5 to 47.25. Under these Re_{probe} conditions, the flow state of MHD flow around a circular cylinder remains stable with no vortex shedding. The length of the recirculation zone ranges from 0.175 to 1.05 mm (Dousset & Pothérat 2008), which is significantly smaller than the 2 mm distance between probes. Consequently, using a spatial resolution of 2 mm, the influence of upstream probes on downstream measurements is negligible.

3.4. *Validation of measurement techniques*

Comprehensive validation tests were conducted to ensure the accuracy and reliability of the present experimental results. For different G/d, Re and Ha, time-averaged velocities U_x and U_0, were determined by the electrical probes and the electromagnetic flowmeter, respectively. The normalized time-averaged velocity (U_x/U_0) and its error bars are plotted in figure 3(a). Under a strong magnetic field ($Ha > 200$), the errors in normalized velocity are less than 5 % and decrease with increasing Ha. However, for $Ha < 200$, the velocity calculated by electrical potential difference is larger than the actual velocity, with a maximum error of less than 20 %. This is related to the correction coefficient c_1 being greater than 1, as induced by the non-negligible induced current (Belyaev *et al.* 2021).

To obtain correlation coefficients and assess the Q2-D or 3-D nature of the flow (see Pothérat & Klein 2014), two probes at the same spatial coordinates (x_0, z_0) were installed on the opposite wall. The probes, extending 2 mm into the core flow across the Hartmann layer, are used to measure potential fluctuations and calculate vertical velocity fluctuations. The vertical velocity fluctuations $u'_z(x_0, y_1, z_0, t_i)$ and $u'_z(x_0, y_2, z_0, t_i)$ are derived to calculate their cross-correlation coefficient (see Klein, Pothérat & Alferenok 2009). The specific formula is as follows:

$$R_{u'_z} = \frac{\sum_{i=1}^{n} (u'_z(x_0, y_1, z_0, t_i) \times u'_z(x_0, y_2, z_0, t_i))}{\sqrt{\sum_{i=1}^{n} (u'_z(x_0, y_1, z_0, t_i))^2 \sum_{i=1}^{n} (u'_z(x_0, y_2, z_0, t_i))^2}} \tag{3.3}$$

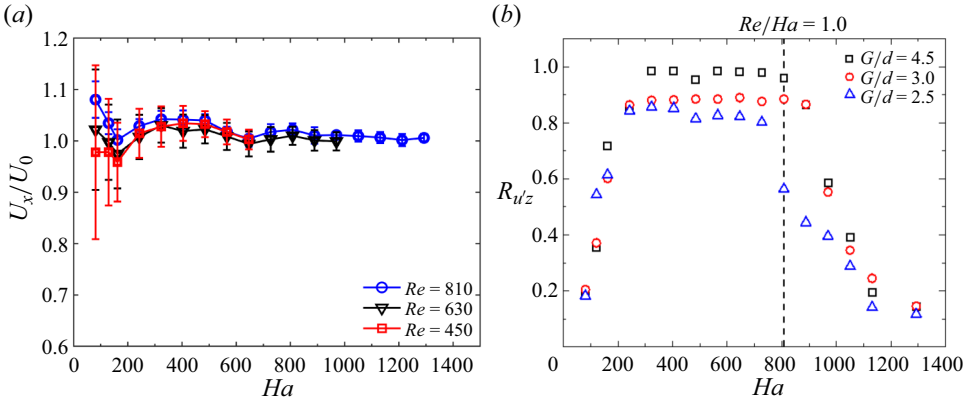

Figure 3. (*a*) Time-averaged velocity calibration for different G/d, Re and Ha. (*b*) The correlation coefficient calculated by u_z' fluctuation versus Ha at $Re = 810$ and $G/d = 2.5$, 3.0, 4.5.

where the coordinates of the vertical velocities are $x_0 = 48$ mm, $y_1 = 2$, $y_2 = 38$ mm and $z_0 = 28$ mm. The sampling number n equals to75 000.

It should be mentioned that the wake street keeps far from the probes when the cylinder is not near the probes. Therefore, the small gap ratios ($G/d = 0.5$–2.0) lead to weak velocity fluctuations in the two probes for the correlation coefficients, resulting in a low signal-to-noise ratio. Consequently, the correlation coefficient $R_{u_z'}$ is only calculated when the cylinder is positioned at $G/d = 2.5$, 3.0 and 4.5 (figure 3*b*).

The correlation coefficient ($R_{u_z'}$) highlights the Q2-D character of the flow under varying magnetic intensities. As figure 3(*b*) reveals, the correlation sustainably increases with the magnetic field when Ha is smaller than 200. The low values of $R_{u_z'}$ at small Ha are attributable to the insufficiently pronounced 2-D character of the shedding vortices. The correlation coefficient $R_{u_z'}$ values increase to values above 0.8 for $200 < Ha < 800$ (for $Ha/Re \sim 0.25$–0.99), indicating a pronounced Q2-D nature of the flow within this range of Ha. However, for Ha greater than 800 (for $Ha/Re \gtrsim 1.0$), there is a notable decrease in $R_{u_z'}$ due to the increasing role of friction in a strong magnetic field within the Hartmann layers, the thickness 'δ_H' of which is proportional to Ha^{-1}. This increase in friction leads to a rapid dissipation of vortices as they move downstream. Furthermore, we note also that the correlations decrease for the given G/d, starting from a value of Re/Ha of the order of unity, which determines the ratio of inertial forces to Hartmann friction forces. Therefore, at $Re/Ha \lesssim 1.0$, there is precisely the predominance of friction forces.

Figure 4 presents critical Reynolds numbers (Re_{cr}) against Ha, aligning well with prior works by Frank *et al.* (2001) and Hussam *et al.* (2011). Frank *et al.* (2001) obtained a critical vortex-shedding parameter (Re_{cr}/Ha) of around 0.47, whereas in this work, Re_{cr}/Ha is in the range of 0.56 ± 0.08. The slight difference may be attributed to the different aspect ratios, with $\alpha = 5$ in Frank's study and $\alpha = 6.67$ in this paper. Additionally, the critical shedding curve exhibits a strong linear relationship with Re/Ha, consistent with conclusions obtained by Frank *et al.* (2001). However, notable discrepancies in Re_{cr}/Ha exist with the findings of Dousset & Pothérat (2008) and Kanaris *et al.* (2013), which are attributed to different blockage ratios ($\beta = 0.1$ in this study, while they had $\beta = 0.25$, see Hussam, Thompson & Sheard 2012).

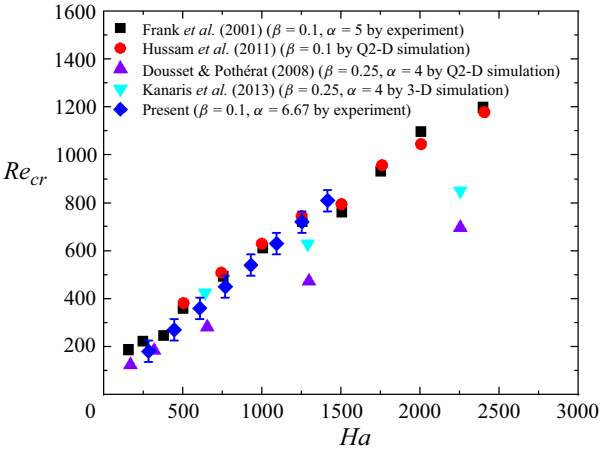

Figure 4. Critical Reynolds numbers (Re_{cr}) against Ha.

4. Results and discussion

Previous research in hydrodynamics indicates that flow around a circular cylinder in proximity to a wall induces secondary vortex shedding from the shear layer near the wall, leading to asymmetry in the velocity profile and the formation of a reverse Kármán vortex street (see Zovatto & Pedrizzetti 2001; He & Wang 2015; Zhou *et al.* 2021). This section investigates the influence of the magnetic field and wall-proximity effect on the MHD flow state and the vortex-shedding regime. A Kármán vortex street, reverse Kármán vortex street and secondary vortices were observed through electrical potential probes. The approach for observing Kármán vortex streets is analogous to that of Rhoads *et al.* (2014). Velocity fluctuations are contoured in both streamwise and vertical directions, whereas Rhoads *et al.* only plotted velocity fluctuations in the streamwise direction with small Ha ($0 < N < 2$). The variation in St should be particularly noteworthy, as it has not been thoroughly analysed until now. The following results examine the effect of wall proximity and the magnetic field on vortex shedding.

4.1. *Impact of the magnetic field on flow regime with weak wall-proximity effect for $G/d = 2.0$*

4.1.1. *Flow regime for $Re = 810$*

As depicted in figures 5 and 6, the contours of dimensional velocity fluctuations show negative values in blue and positive values in red. According to the classical theory of the Kármán vortex street (see Williamson 1996), vortices shedding from the upper surface of the cylinder follow a clockwise rotation, inducing positive velocity fluctuations on the upper side and negative velocity fluctuations on the lower side of these vortices. Conversely, vortices shedding from the lower surface of the cylinder exhibit a counterclockwise rotation, resulting in negative velocity fluctuations on the upper side and positive velocity fluctuations on the lower side. Similar conclusions can be drawn for velocity fluctuations on the left and right sides of the vortices. Therefore, the alternating pattern of positive and negative velocity fluctuations aligns with the Kármán vortex street.

For $81 \leq Ha \leq 323$ (see figures 5*a*,*b* and 6*a*,*b*), the intensity of the vortices rises with a stronger magnetic field. This enhancement is due to the augmented two-dimensionality of the vortices and a corresponding decrease in Joule dissipation. Consequently, the vortices

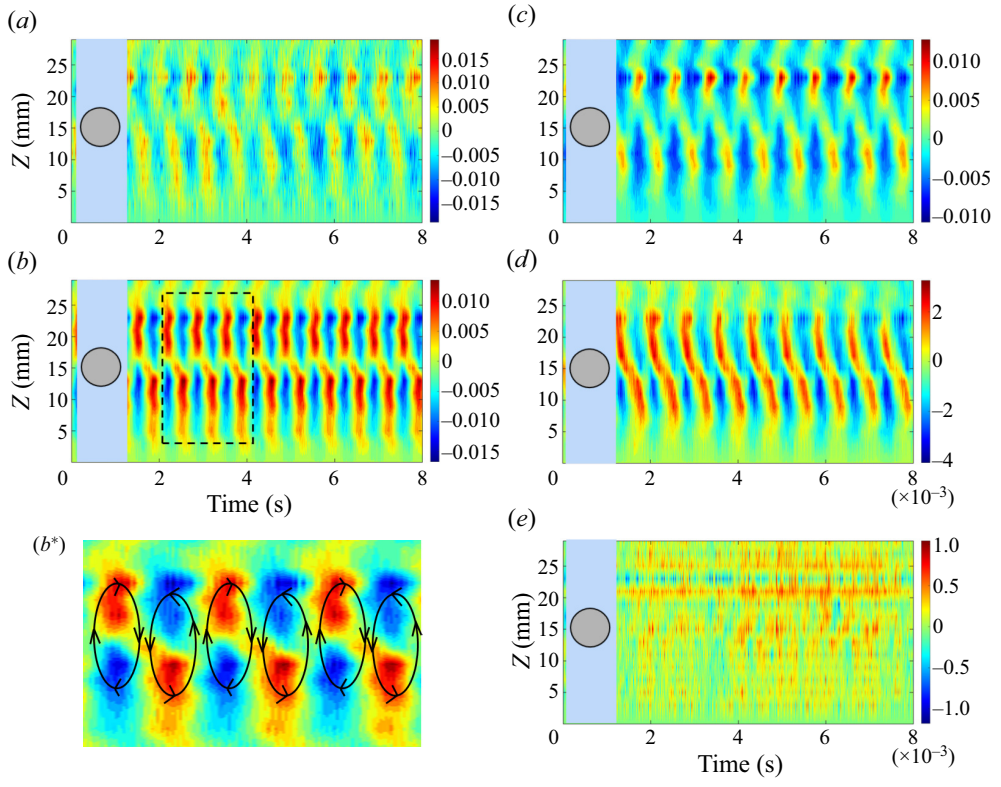

Figure 5. Contour map of velocity fluctuations u_x' with varying magnetic fields for $G/d = 2.0$ at $x = 7.5d$. Panels show (*a*) $Ha = 81$, $Re/Ha = 10.0$, (*b*) $Ha = 323$, $Re/Ha = 2.50$, (*c*) $Ha = 646$, $Re/Ha = 1.24$, (*d*) $Ha = 969$, $Re/Ha = 0.84$ and (*e*) $Ha = 1131$, $Re/Ha = 0.72$.

become more regular, robust and coherent as the magnetic field increases. Enlarged fragments of the Kármán vortex street are depicted in figures 5(*b**) and 6(*b**).

For $323 \leq Ha \leq 646$, an increase in magnetic field strength leads to reduced intensity (see figures 5*b*,*c* and 5*b*,*c*) and frequency of vortex shedding (see also figure 7*b*,*c*). This reduction is attributed to the enhanced influence of Hartmann friction, which affects both the formation of vortices immediately behind the cylinder and their propagation downstream to the measuring cross-section.

For $646 \leq Ha \leq 969$ (see figures 5*c*,*d* and 6*c*,*d*), the amplitude of velocity fluctuations decreases with the rising magnetic field, which is attributed to the suppression of vortex shedding by the field behind the cylinder. At a certain distance from the cylinder, vortices arise due to K-H-type instability in the velocity shear region in the wake. Furthermore, the frequency of vortices noticeably increases, apparently due to the narrowing of the wake behind the cylinder.

For $969 < Ha \leq 1131$ (see figures 5*d*,*e* and 6*d*,*e*), the increasing magnetic field rapidly dissipates the vortex intensity. The oscillation of the wake is almost completely suppressed by a sufficiently strong magnetic field. The velocity fluctuations are nearly dissipated by Hartmann friction, with only slight and irregular vertical velocity fluctuations u_z'.

Consequently, for $Ha \geq 1131$, periodic shedding is unobservable at $x = 7.5d$ (figures 5*e* and 6*e*). Only weak transverse velocity fluctuations of an intermittent character are visible, and no prominent peak is observed in the spectrum (figure 7*e*).

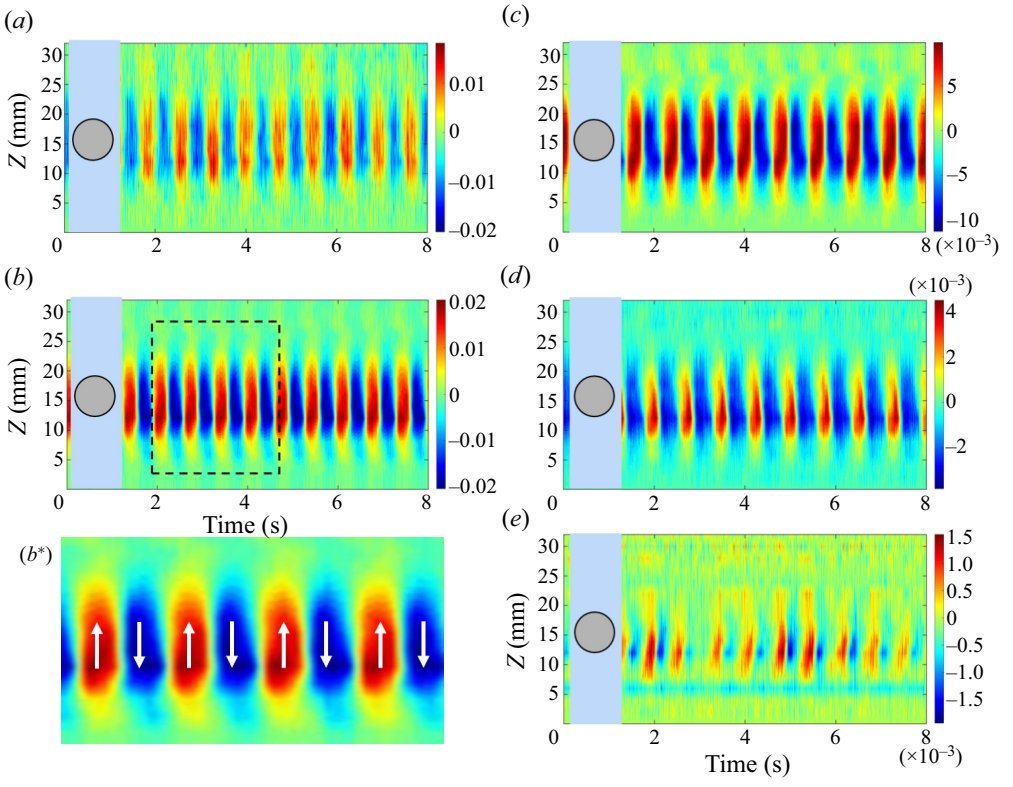

Figure 6. Contour maps of velocity fluctuations u_z' with varying magnetic fields for $G/d = 2.0$ at $x = 7.5d$. Panels show (*a*) $Ha = 81$, $Re/Ha = 10.0$, (*b*) $Ha = 323$, $Re/Ha = 2.50$, (*c*) $Ha = 646$, $Re/Ha = 1.24$, (*d*) $Ha = 969$, $Re/Ha = 0.84$ and (*e*) $Ha = 1131$, $Re/Ha = 0.72$.

The point with the maximum vertical velocity fluctuation $(u_z')_{rms}$ is used for the power spectral density (PSD) analysis (figure 7). The peak points of the vertical component u_z' are located near the coordinate $z = 15$ mm, corresponding to the position of the cylinder axis (figure 8*b*). The two peak values of the streamwise component u_x' are located on both sides of this coordinate (figure 8*a*). This observation aligns with classical theories in vortex dynamics (Zdravkovich 1997), predicting the distribution of velocity pulsation intensities in the wake of a vortex street. Both the fundamental shedding frequency and its corresponding harmonics are observed in the spectrum, resulting from the alternating shedding vortices and wake oscillations.

At $Ha = 161$ (figure 7*a*), the spectrum exhibits a power decay rate of $-5/3$, indicating that 3-D flow is prominent. As the magnetic field increases to $Ha = 323$ (figure 7*b*), the order of energy amplifies from 10^{-4} to 10^{-3}, the shedding frequency slightly increases and the flow transitions to a Q2-D flow state with a decay rate approaching -3. With increasing magnetic field, the shedding frequency initially decreases and then increases (figure 7*b–d*). For $Ha = 1131$ (figure 7*e*), the slope of the decay rate approaches -3 but with no dominant peak for frequency, consistent with figures 5(*e*) and 6(*e*). The energy order falls from 10^{-3} to 10^{-7} as the magnetic field changes from $Ha = 323$ to $Ha = 1131$.

The variation in the intensity of velocity fluctuations across the transverse direction reflects the spanwise distance and strength of vortices. In figure 8, the root-mean-square (r.m.s.) of velocity is presented under various magnetic fields, showing a consistent trend

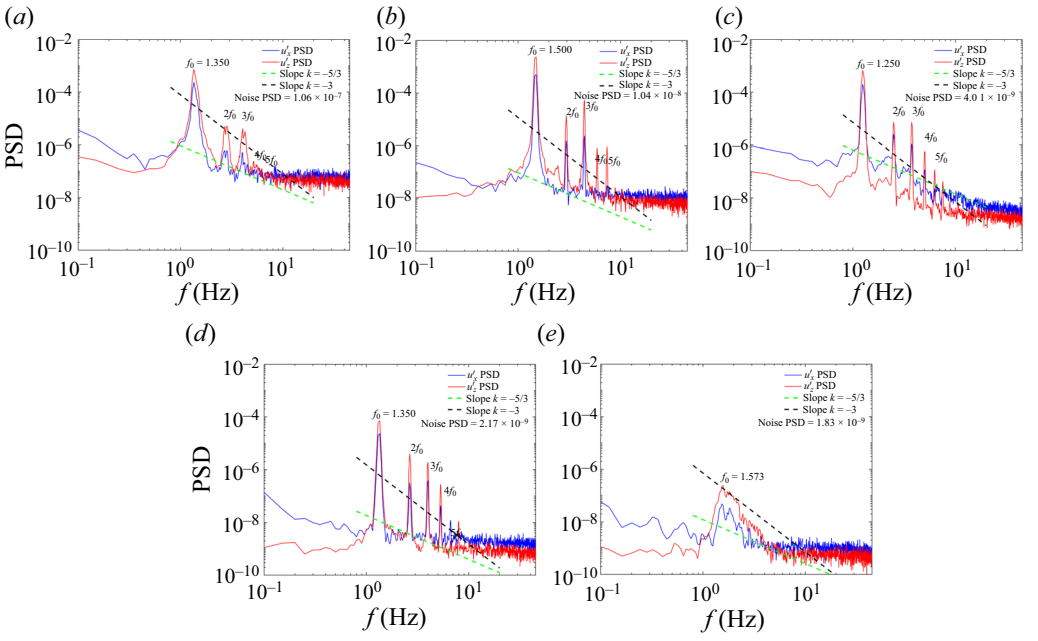

Figure 7. Spectra of u'_x and u'_z corresponding to the point of maximum $(u'_z)_{rms}$ velocity fluctuations ($G/d = 2.0$). Panels show (*a*) $Ha = 81$, $Re/Ha = 10.0$, (*b*) $Ha = 323$, $Re/Ha = 2.50$, (*c*) $Ha = 646$, $Re/Ha = 1.24$, (*d*) $Ha = 969$, $Re/Ha = 0.84$ and (*e*) $Ha = 1131$, $Re/Ha = 0.72$.

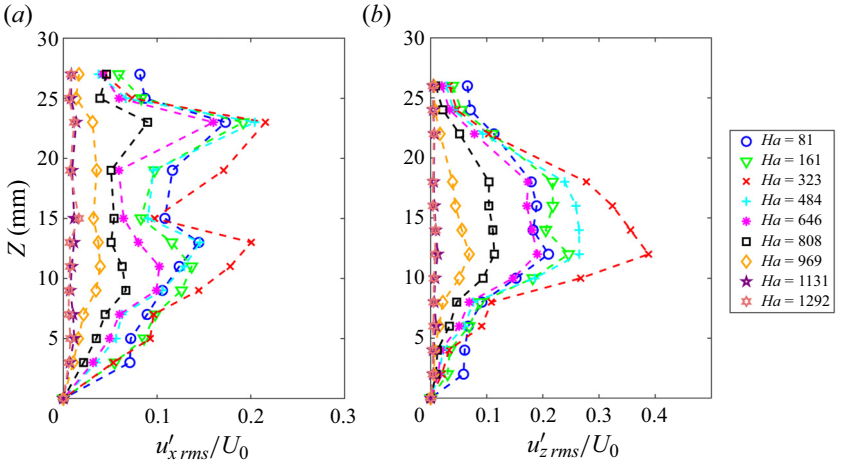

Figure 8. The r.m.s. of non-dimensional velocity fluctuations $(u'_x)_{rms}$ and $(u'_z)_{rms}$ under different magnetic fields ($G/d = 2.0$, at $x = 7.5d$).

with the energy of the vortices. For $G/d = 2.0$, the r.m.s. of velocity fluctuations increases with the magnetic field from $Ha = 81$ to 323. This increase of vortex intensity is related to the transition from 3-D flow to Q2-D flow, accompanied by the energy transport from small-scale vortices to large-scale vortices. However, further increment of the magnetic field for $Ha > 323$ results in a decrease in velocity fluctuations, which is due to the dissipation of the Hartmann friction. When $B \geq 0.7$ T ($Ha \geq 1131$), the r.m.s. of velocity

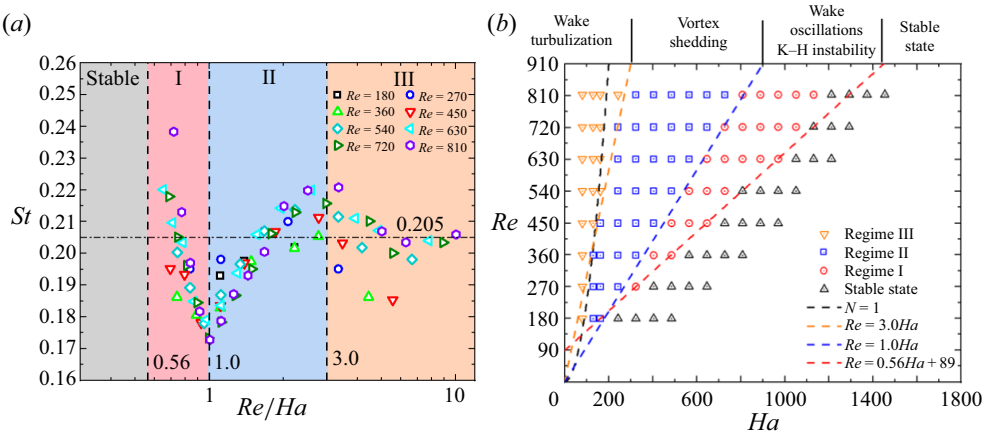

Figure 9. (*a*) Relationship between *St* and *Re*/*Ha*. (*b*) Phase diagram (for $G/d = 2.0$).

fluctuations approaches a near-zero value, indicating that vortex shedding is completely suppressed or dissipated at $x = 7.5d$.

According to the theory of the vortex wake behind a cylinder, the centres of the wake street correspond to local maxima in the r.m.s. values of the vertical velocity fluctuations u_z'. As shown in figures 5 and 6, the vertical velocity fluctuations u_z' are predominantly concentrated in the height range of $z = 9$–21 mm (equivalent to $2d$), while the amplitude of the velocity fluctuations rapidly decreases beyond this range. However, the influence of the streamwise velocity fluctuations extends over a greater range of $z = 5$–25 mm (approximately $3.3d$), beyond which the velocity fluctuations decrease more slowly. Furthermore, the magnetic field not only dissipates the energy of the vortices but also narrows the vortex street (figure 6).

4.1.2. *Vortex-shedding frequency and phase diagram for Re = 180–810*

The relationship between the Strouhal number (*St*) and the ratio *Re*/*Ha* is depicted in figure 9(*a*). In weak magnetic fields, the trend of *St* changing to *Re*/*Ha* is similar to the relationship between *St* and *Re* in hydrodynamics. Under moderate magnetic fields, *St* increases with increasing flow rate and decreasing magnetic field for $Re/Ha \gtrsim 1$. However, *St* increases with *Re*/*Ha* under strong magnetic fields ($Re/Ha \lesssim 1$).

The flow regimes are often defined by the fluctuations, spectra and frequency of the velocity. In this research, the regimes of vortex shedding are categorized into three different regimes based on the trend of *St* against *Re*/*Ha*, excluding the 'stable state' (see figure 9*b*), which are defined and analysed as follows:

(i) Regime I, for $0.56 \lesssim Re/Ha \lesssim 1.0$ – 'oscillations of attached vortices and wake shear layers', dominated by the Lorentz force and Hartmann friction (for $808 < Ha < 1131$, at $Re = 810$). In the regions $Re/Ha \lesssim 1.0$, the frequency of vortex shedding increases with growing *Ha*. Notably, the order of vortex energy remains above 10^{-4} for $Re/Ha \gtrsim 1.0$ (figure 7*a*–*c*), but it drops suddenly down during $Re/Ha \lesssim 1.0$ (figure 7*d*,*e*). This change comes from the different vortex-shedding regimes. Although previous researchers (Andreev & Kolesnikov 1998; Frank *et al.* 2001; Dousset & Pothérat 2012) observed the nonlinear variations of the physical parameters against magnetic field strength, they did not attribute these phenomena to a new mode of vortex shedding.

Andreev & Kolesnikov (1998) noted that the magnetic field delays the separation of vortices but does not suppress the instability of the extended shear layer, explaining the increase of vortex-shedding frequency in a narrowing wake with an increasing magnetic field. In this work, the contour maps show regular vortex shedding at $x = 7.5d$ in this regime (figures 5*d*,*e* and 6*d*,*e*). The vortices shed from the oscillating shear layer due to the K-H instability. It can be confirmed that the parameter range for the existence of the shear layer oscillation is broad ($Re \sim 270$–810, $Ha \sim 323$–1131). With a sufficiently strong magnetic field ($Ha >> Re$), the wake vortex oscillation is completely suppressed, leaving two attached vortices at the rear of the cylinder with no vortex generation.

The primary difference between the vortex-shedding modes under strong and weak magnetic fields lies in the vortex generation mechanism. In regime I, as Ha increases, the flow around the cylinder experiences additional intensified dissipation mechanisms associated with Hartmann friction and Joule dissipation. These mechanisms broaden the range of the Re/Ha parameter values for transient processes compared with those without a magnetic field. At high Ha, the oscillations of the attached vortices and the wake occur. In this scenario, the vortex street is narrowed and the vortex intensity is significantly reduced. Vortex detachment occurs at the tail of the shear layer, and the pressure difference on both the upper and lower sides of the cylinder approaches zero. The shear layers are stretched, causing the recirculation length to extend up to $2d$ due to the negative velocity in the recirculation zone, which leads to a streamwise Lorentz force. The viscous force and Lorentz force balance each other within the stretched shear layer. The vortices are shed from the oscillating shear layers due to K-H instability (figures 6*d* and 6*e*), rather than pressure difference. Moreover, as Ha decreases, K-H-type shear instability develops along the wake with the formation of vortices at a certain distance from the cylinder. These vortices were detected by the measuring sensor at the distance of $x = 7.5d$. With a further decrease in Ha, the point of vortex formation moves closer to the cylinder, and when $Re/Ha \lesssim 1.0$, the vortices are shed directly by the cylinder (figure 9*a*).

(ii) Regime II, for $1.0 \lesssim Re/Ha \lesssim 2.50$ – Q2-D vortex shedding', characterized by a competition between Lorentz force and inertia force (for $323 \lesssim Ha \lesssim 808$, at $Re = 810$). For $Re/Ha \gtrsim 1.0$, both the Strouhal number and vortex intensity increase with increasing Re/Ha. As the magnetic field decreases (resulting in an increase in Re/Ha), vortex detachment occurs on the cylinder's surface due to the combined action of pressure, viscous forces and Lorentz forces within the boundary layer. This detachment is primarily caused by a pressure differential that leads to the separation of the boundary layer. The vortices appear barrel-like (or cigar-like) in shape, as observed by Mück *et al.* (2000). Additionally, the vortices maintain a column-like shape along the streamwise direction for a moderate magnetic field, perfectly satisfying the condition of the Q2-D model. Therefore, this vortex-shedding regime should be considered a Q2-D mode during the formation of Kármán street under a moderate magnetic field (figures 6*b* and 6*c*).

(iii) Regime III, for $Re/Ha \gtrsim 2.50$ – 'transition of magnetohydrodynamic to hydrodynamic Kármán street', dominated by the inertia force (for $Ha \leq 323$, at $Re = 810$). In this regime, as Re/Ha increases, the inertia force tends to exceed the Lorentz force, resulting in the transition from Q2-D flow to 3-D flow. The coherent Q2-D columnar vortex breaks down into smaller 3-D vortices with increasing Re/Ha, and the effect of Joule dissipation becomes increasingly significant (figures 6*a*). Additionally, the frequency of vortex shedding exhibits a slight increase with rising Re. In this regime, the vortex-shedding frequency shows a non-monotonic variation, potentially analogous to transition modes observed in ordinary hydrodynamics. As noted by Williamson (1996), the transformation of vortex-shedding modes results in energy transport, involving the transfer

of energy from 2-D columnar vortex structures to 3-D vortex configurations, accompanied by the decrease of the correlation coefficient for $Re/Ha \gtrsim 2.04$ (figure 3(*b*) for $Ha < 400$).

4.2. *Impact of the magnetic field on flow regime with strong wall-proximity effect for $G/d = 0.5$*

4.2.1. *Flow regime for $Re = 810$*

The wall-proximity effect for $G/d = 0.5$, compared with $G/d = 2.0$, leads to significant differences in vortex dynamics characteristics. At $Ha = 81$ (figures 10*a* and 11*a*), the trajectory of the vortex street exhibits slight vertical undulations with the vortex core oscillating near $z = 10$ mm (the centre of the cylinder is at $z = 6$ mm). The vortex structure appears irregular, with numerous small vortices present. These undulations and irregular shedding of vortices in the vortex street may be attributed to unsteady variations in the size of the recirculation region near the wall, which strongly affect the interaction and trajectory of the vortices. Additionally, the velocity fluctuations near the wall at $G/d = 2.0$ (figures 5 and 6) are significantly larger than those at $G/d = 0.5$ (figures 10 and 11). This observation further supports the presence of a strong interaction between the Kármán vortex street and the wall-proximity effect.

As the magnetic field increases to $Ha = 323$–646 (figures 10*b*,*c*, *c** and 11*b*,*c*, *c**), the vortices become more regular and coherent, indicating an increase in vortex energy. Additionally, the undulating motion of the vortices is entirely suppressed, which is attributed to the control of the recirculation region near the wall by the magnetic field. Interestingly, the centres of the clockwise vortices on the upper side are lower than those of the counterclockwise vortices on the lower side, indicating a phenomenon of reverse Kármán Street. The lower wake vortex with positive vorticity moves away from the wall and even surpasses the height of the upper wake vortex with negative vorticity. This phenomenon suggests that the wall-proximity effect, like the recirculation region near the wall, bounces the counterclockwise vortices away from the wall. In hydrodynamic flow, the instability of the wall shear layers leading to secondary vortices is also observed at $G/d = 0.5$–1.5 in previous literature. However, secondary vortex shedding from the wall boundary layer was not observed at $x = 7.5d$. The reason is that the secondary vortices have a strong vertical velocity component and rapidly dissipate through interactions with the upper and lower side vortices.

In the range of $646 < Ha \leq 969$, secondary vortices are detected by the electrical probes (figures 10*d*, *d** and 11*d*, *d**). The clockwise secondary vortices separate from the boundary layer. These vortices interact strongly with the vortices shedding from the cylinder. As shown in figures 10(*d**) and 11(*d**), the centres of the secondary vortices are positioned below the counterclockwise vortices from the lower shear layer, while the centres of the clockwise vortices from the upper shear layer are higher. Additionally, the secondary vortices are connected to the vortices shedding from the cylinder in figure 10(*d*,*e*), indicating strong and direct interactions with both sides of the shedding vortices. The secondary vortices periodically shed from the wall boundary layer. Consequently, the PSD of the velocity fluctuations (see figure 12*d*) contains higher-order harmonics of the vortex-shedding frequency than the PSD with no secondary vortices.

Additionally, the height of the vortex street's impact reduces from $4d$ to $2d$. This change indicates that a strong magnetic field not only narrows the vortex street but also suppresses the size of recirculation region near the wall, resulting in a reduction in the z-direction velocity component of the vortices.

In the range of $1131 \leq Ha \leq 1292$, the vortex intensity and velocity fluctuations become weak (figures 10*e*,*f* and 11*e*,*f*), attributed to the significant dissipation effects under a

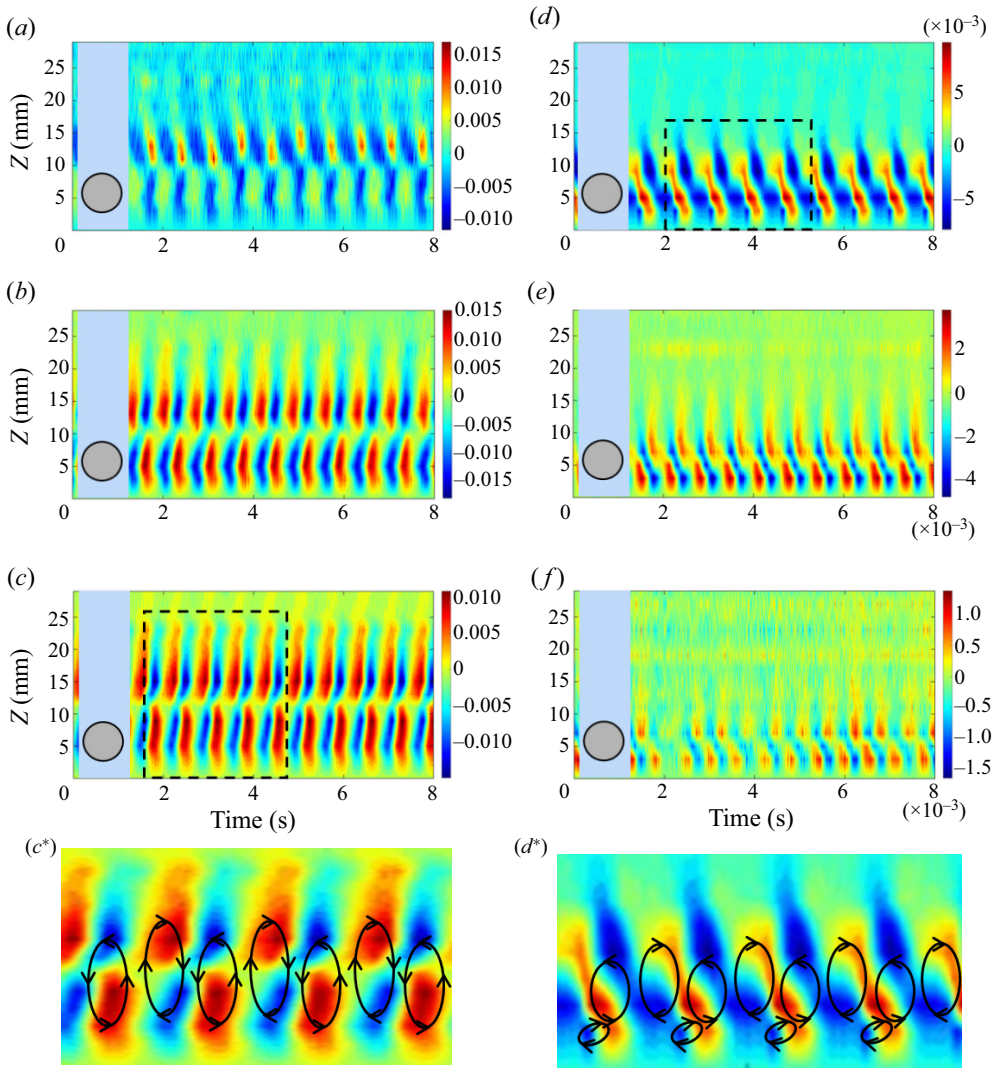

Figure 10. Contour maps of velocity fluctuations u_x' with varying magnetic fields for $G/d = 0.5$ at $x = 7.5d$. Panels show (*a*) $Ha = 81$, $Re/Ha = 10.0$, (*b*) $Ha = 323$, $Re/Ha = 2.50$, (*c*) $Ha = 646$, $Re/Ha = 1.24$, (*d*) $Ha = 969$, $Re/Ha = 0.84$, (*e*) $Ha = 1131$, $Re/Ha = 0.72$ and (*f*) $Ha = 1292$, $Re/Ha = 0.64$.

strong magnetic field. However, at $G/d = 2.0$, the same magnetic field nearly suppresses the velocity fluctuations entirely. The instability of vortex shedding is influenced by the wall-proximity effect. In hydrodynamic flow, the wall-proximity effect inhibits vortex shedding. However, under a magnetic field, the wall-proximity effect promotes the vortices shedding from the cylinder's shear layers, which is discussed in detail later. Additionally, as the magnetic field strength increases ($1131 \leq Ha \leq 1292$), the instability of the Shercliff layer is initially suppressed. With further increased magnetic field strength ($Ha > 1616$), the instability of the wake is completely suppressed.

It is noteworthy that, at a low magnetic field ($Re/Ha = 10.0$, figures 10*a* and 11*a*), the central axis of the vortex street rises to $z = 12$ mm at the cross-section $x/d = 7.5$, where the measurement sensor is located. However, with an increase in Ha ($Re/Ha < 0.84$,

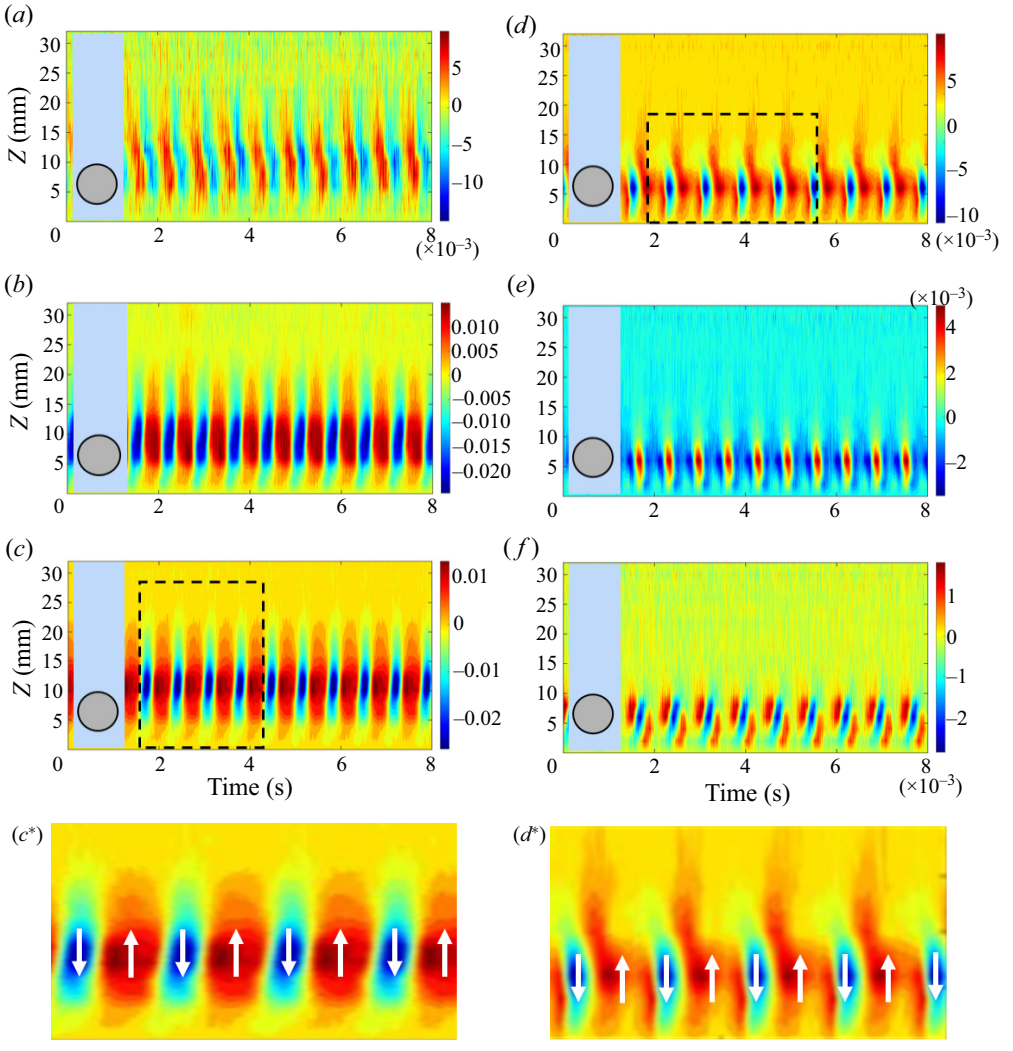

Figure 11. Contour maps of velocity fluctuations u_z' with varying magnetic field for $G/d = 0.5$ at $x = 7.5d$. Panels show (*a*) $Ha = 81$, $Re/Ha = 10.0$, (*b*) $Ha = 323$, $Re/Ha = 2.50$, (*c*) $Ha = 646$, $Re/Ha = 1.24$, (*d*) $Ha = 969$, $Re/Ha = 0.84$, (*e*) $Ha = 1131$, $Re/Ha = 0.72$ and (*f*) $Ha = 1292$, $Re/Ha = 0.64$.

figures 10*d–f* and 11*d–f*), the wake is pressed to the bottom wall, approaching $z = 6$ mm, in a regime dominated by K-H instability (see also the discussion about figure 14).

Figure 12 provides spectral information on the vortex-shedding frequency and velocity fluctuations near the wall. The vortex-shedding frequency near the wall also shows a trend of first decreasing and then increasing with the magnetic field. For $G/d = 0.5$, the trends of St with Ha have a consistent tendency with $G/d = 2.0$. However, the critical Re/Ha for the trend of the shedding frequency differs, attributed to the strong interaction between the wall boundary layer and the cylinder's shear layers.

An intriguing phenomenon, numerous harmonic frequencies (up to ten or more), is observed in the spectrum at $Ha = 969.6$ for $G/D = 0.5$ (figure 12*d*). This phenomenon also occurs at $G/d = 1.0$ but not at $G/d \geq 1.5$, suggesting that secondary vortices are induced by a strong wall-proximity effect. However, the secondary vortices are also influenced by the

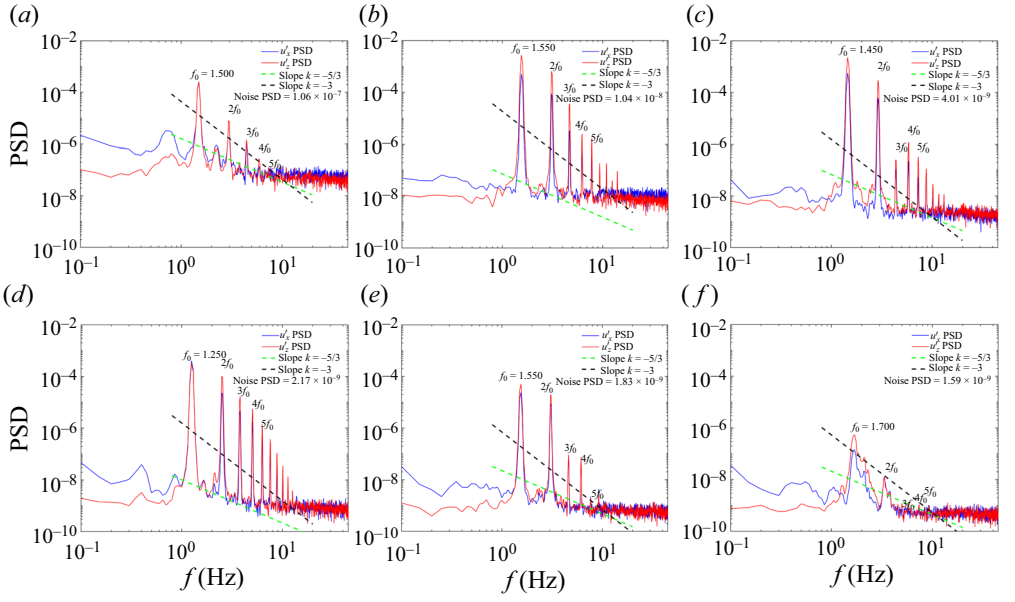

Figure 12. Spectra of u'_x and u'_z corresponding to the point of maximum u'_z velocity fluctuations ($G/d = 0.5$). Panels show (*a*) $Ha = 81$, $Re/Ha = 10.0$, (*b*) $Ha = 323$, $Re/Ha = 2.50$, (*c*) $Ha = 646$, $Re/Ha = 1.24$, (*d*) $Ha = 969$, $Re/Ha = 0.84$, (*e*) $Ha = 1131$, $Re/Ha = 0.72$ and (*f*) $Ha = 1292$, $Re/Ha = 0.64$.

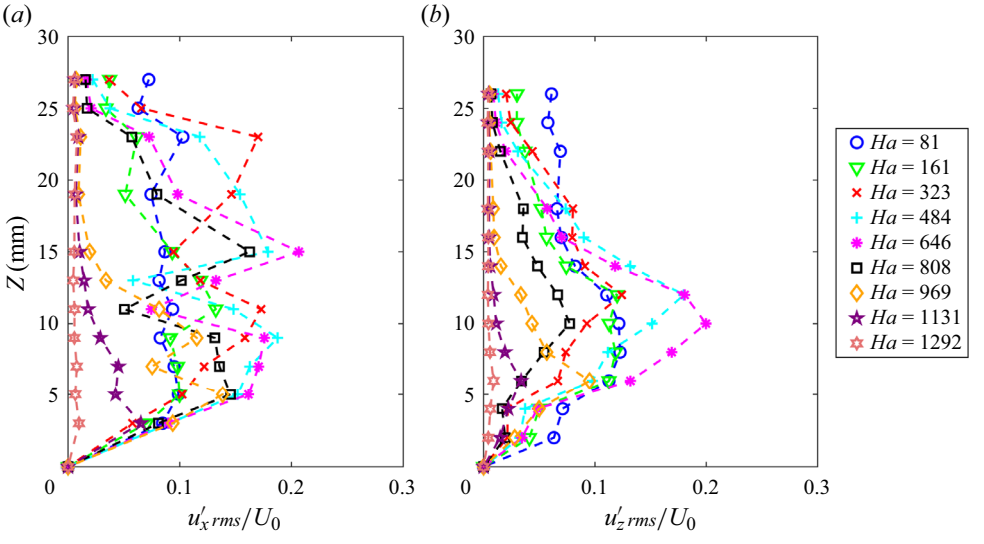

Figure 13. The r.m.s. of non-dimensional velocity fluctuations $u'_{x\,rms}$ and $u'_{z\,rms}$ under different magnetic fields ($G/d = 0.5$, at $x = 7.5d$).

magnetic field as figures 11(*e*) and 11(*f*) (no secondary vortices). Furthermore, the scaling decay rates of −5/3 and −3 are marked as references in the spectrum.

With the wall-proximity effect, the r.m.s. values of streamwise velocity fluctuations $(u'_x)_{rms}$ and vertical velocity fluctuations $(u'_z)_{rms}$ are illustrated in figure 13. Comparing the u'_{rms} profiles between $G/d = 2.0$ and $G/d = 0.5$ (figures 8 and 13), the r.m.s. of velocity fluctuations peaks at $Ha = 323.2$ for $G/d = 2.0$. However, the maximum r.m.s. occurs at $Ha = 646.4$ for $G/d = 0.5$. The order of velocity fluctuation energy increases from 10^{-4}

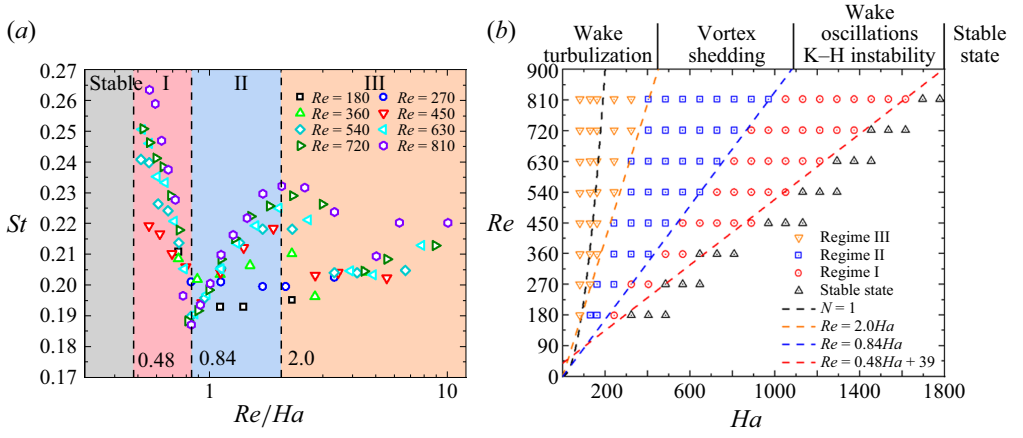

Figure 14. (*a*) Relationship between *St* and *Re*/*Ha*. (*b*) Phase diagram (for $G/d = 0.5$).

to 10^{-3} as the magnetic field increases from 80.8 to 646.4(figure 12*a–c*). Additionally, for $1131.2 \leq Ha \leq 1292.8$ at $G/d = 0.5$, significant velocity fluctuations still exist rather than approaching zero due to the influence of the wall-proximity effect. Furthermore, the vertical location of the peak velocity fluctuation $(u'_{z\,rms})_{max}$ decreases as the magnetic field increases, due to a change in the trajectory of vortex motion with the increasing magnetic field. The order of velocity fluctuation energy decreases from 10^{-3} to 10^{-5} as the magnetic field increases from $Ha = 646.4$ to $Ha = 1292.8$ (figure 12*c–f*).

4.2.2. *Vortex-shedding frequency and phase diagram for Re = 180–810*

The results of the flow around a cylinder at $G/d = 0.5$ demonstrate that the wall-proximity effect significantly impacts on the vortex-shedding regime. The vortex-shedding regimes are also categorized into three regimes against *Re*/*Ha*, excluding the 'stable state'. The three regimes are as with $G/d = 2.0$ (see figure 14), but with different critical *Re*/*Ha*. The differences from the $G/d = 2.0$ are discussed below:

(i) Regime I, for $0.48 \lesssim Re/Ha \lesssim 0.84$ (for $969 \leq Ha \leq 1616$, at $Re = 810$). The vortex-shedding frequency and vortex energy at $G/d = 0.5$ are larger than those of $G/d = 2.0$ due to the wall-proximity effect, consistent with findings in hydrodynamics. With the magnetic field increases, similar to the conditions at $G/d = 2.0$, the vortex-shedding frequency increases and the energy of the vortices sharply declines. Additionally, the vortex street extends along the streamwise direction with no vertical velocity due to the suppression of secondary vortices near the wall by the strong magnetic field (figures 11*e* and 11*f*).

The transition from the 'stable state' to regime I is facilitated by the Shercliff layer effect under magnetic fields, which reduces the critical *Re*/*Ha* values. In other words, the wall-proximity effect intensifies the shear layer's K-H instability, promoting vortex shedding at a given *Re*/*Ha*. However, the wall-proximity effect always suppresses or delays the vortex shedding in hydrodynamics. Therefore, conclusions drawn under magnetic fields are contrary to those in hydrodynamics, potentially due to the Shercliff layer effect induced by magnetic fields. In contrast, under a strong magnetic field, the Shercliff layer effect promotes vortex shedding by causing disturbances, thereby enhancing the instability of oscillating shear layers. Consequently, the critical parameter *Re*/*Ha* for vortex shedding decreases from 0.64 (at $G/d = 2.0$) to 0.48 (at $G/d = 0.5$) under the Shercliff layer effect.

Regarding the transition from regime II to regime I, due to the wall-proximity effect in hydrodynamics, the flow separation points on the cylinder surface move downstream. This effect accelerates the movement of the flow separation point from the cylinder surface to the tail of the shear layer. As a result, the critical Re/Ha for the transition from vortex-shedding mode II to I decreases from 1.0 to 0.84. Therefore, it is the Shercliff layer effect that results in a decrease in the critical value of Re/Ha.

(ii) Regime II, for $0.84 \lesssim Re/Ha \lesssim 2.0$ (for $404 \leq Ha \leq 969$, at $Re = 810$). In regime II, columnar vortex shedding occurs at the cylinder surface caused by the pressure differential of the cylinder surface. With an increasing magnetic field (resulting in a decrease of Re/Ha), both the vortex-shedding frequency and vortex intensity decrease. Unlike at $G/d = 2.0$, the wall-proximity effect under these conditions induces secondary vortices on the wall, altering the trajectory of the cylinder's vortex street (figures 11*c* and 11*d*) and introducing higher harmonics to the frequency spectrum (figures 12*c* and 12*d*).

Periodic separation of the wall boundary layer is induced by a reverse pressure gradient on the downstream wall, leading to the shedding of secondary vortices. At $Ha = 969$, the interaction between secondary vortices and the wake is observed. These secondary vortices result in a strong vertical velocity component of the cylinder's wake vortices, pushing the vortices away from the cylinder's central height (figures 11*c* and 11*d*). The intense interaction between the cylinder's wake vortices and secondary vortices leads to 'vortex pairing' phenomenon (figures 10*d* and 11*d*), which contributes to the emergence of higher harmonics in the flow field (figures 12*c* and 12*d*).

The flow dynamics involves complex interactions among the cylinder shear layers, Hartmann layer and Shercliff layer. Induced currents within these layers lead to 3-D effects in the flow. With the addition of the Shercliff layer effect, a stronger magnetic field is required to transition from 3-D flow to Q2-D flow. Consequently, the critical Re/Ha for the transition from regime III to regime II decreases from 2.5 to 2.0.

Notably, Chatterjee & Gupta (2015) observed that secondary vortex shedding occurs within the Shercliff layer under the influence of a magnetic field when the cylinder blockage ratio $\beta = 0.25$. The present study could not determine the precise critical value (Re_{cr}/Ha) for the Shercliff layer's instability and secondary vortex shedding, as the probe at $x = 7.5d$ is relatively far from the cylinder. However, it can be inferred that the instabilities of the Shercliff layer and the shear layers on both sides of the cylinder correspond to different critical Re_{cr}/Ha values. Initially, the magnetic field suppresses the secondary vortices of the Shercliff layer ($Re_{cr}/Ha \lesssim 0.84$, figure 11*e*,*f*) and eventually suppresses the instability of the cylinder's shear layers ($Re_{cr}/Ha \lesssim 0.48$, figure 14).

(iii) Regime III, for $Re/Ha \gtrsim 2.0$ (for $Ha \leq 404$, at $Re = 810$). In regime III, the inertia force significantly outweighs the Lorentz force, facilitating the transition from Q2-D flow to 3-D flow. The vortices transform from the columnar shape to small 3-D structures due to the Joule dissipation effect, resulting in an energy decrease in the main wake vortices. Owing to the strong wall-proximity effect, the additional 3-D effect reduces the critical Re_{cr}/Ha from regime II to regime III ($Re_{cr}/Ha = 2.0$ for $G/d = 0.5$, $Re_{cr}/Ha = 3.0$ for $G/d = 2.0$). In other words, the instability of the Shercliff layer makes the Q2-D columnar vortices more likely to break down into 3-D small-scale vortices.

At higher Reynolds numbers, changes in the vortex-shedding frequency exhibit a 'jump' (for $270 \leq Re \leq 810$ in figure 14*a*). In hydrodynamics, an increase in Reynolds number typically raises the vortex-shedding frequency. However, the frequency 'jump' occurs during the transition from laminar to turbulent flow, which is associated with energy transport processes.

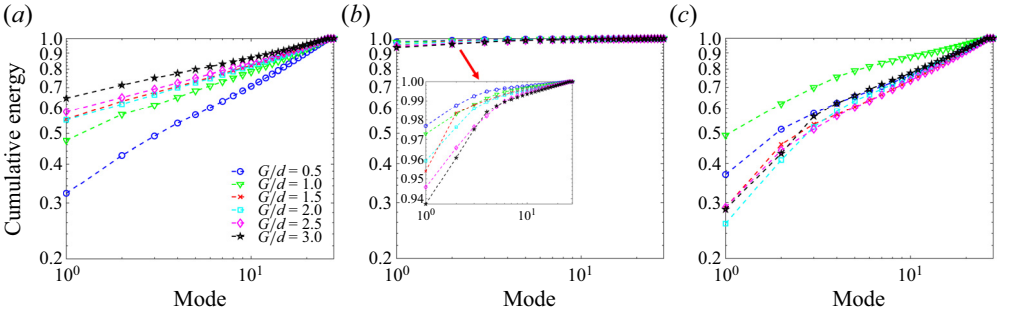

Figure 15. Cumulative energy for different G/d at $Re = 810$. Panels show (*a*) $Ha = 161$, $Re/Ha = 5.02$, regime III, (*b*) $Ha = 646$, $Re/Ha = 1.24$, regime II and (*c*) $Ha = 1131$, $Re/Ha = 0.72$, regime I.

4.3. *The wall-proximity effect on MHD flow using proper orthogonal decomposition*

Proper orthogonal decomposition (POD) is a powerful tool for uncovering the mechanisms of complex flows and simplifying the analysis of fluid dynamics problems. This section focuses on analysing the modal contribution and the diagram of the first two modal coefficients. The effect of G/d on fluid dynamics and flow structures is examined using POD.

4.3.1. *Wall-proximity effect on mode energy*

In figure 15(*a*), the energy of the first mode in regime III, dominated by inertial forces, increases with G/d, consistent with the conclusions obtained by Zhou *et al.* (2021). When the magnetic field is increased to $Ha = 646$, the magnetic field transfers the energy of small vortices in 3-D flow to 2-D columnar vortices, resulting in the first mode energy increasing to 90 %. Under the influence of the wall-proximity effect, as shown in figure 15(*b*), the energy of the first mode decreases with the increase of G/d. As the magnetic field is further increased to $Ha = 1131$, vortex shedding occurs only for $G/d = 0.5$ and 1.0. Although there is no shedding for $G/d \geq 1.5$, energy decay caused by velocity fluctuations is still observed (see figure 7*e*). Therefore, in figure 15(*c*), the energy of the first mode for $G/d = 0.5$ and 1.0 is higher than $\approx$40 %, while the energy proportion of the first mode for $G/d \geq 1.5$ is less than 30 %.

4.3.2. *Wall-proximity effect on mode coefficients and phase diagrams*

The trajectory of the first two modal coefficients in the classic Kármán vortex street is circular. The amplitude of the first two modal coefficients is essentially identical, differing only by a certain phase, indicating that the first two modes correspond to the alternate shedding of vortices on the upper and lower sides of the cylinder. However, small-scale vortices and other factors like turbulence disrupt the regularity of the circular shape.

When the magnetic field is low, as shown in figure 16(*i*), the flow contains many small-scale vortices, and the 3-D effects cause numerous minor fluctuations in the modal coefficient curve. The irregular shape of the trajectory of the first two modal coefficients indicates a weak correlation between the first two modes when 3-D effects are significant.

As the magnetic field increases, the flow transitions to a Q2-D flow state, corresponding to regime II (figure 16(ii)). The main vortex structure becomes more regular and coherent (figures 5*d* and 10*b*), making the modal coefficient curve more regular and periodic. The phase diagram forms a closed and irregular ring, indicating good periodicity and

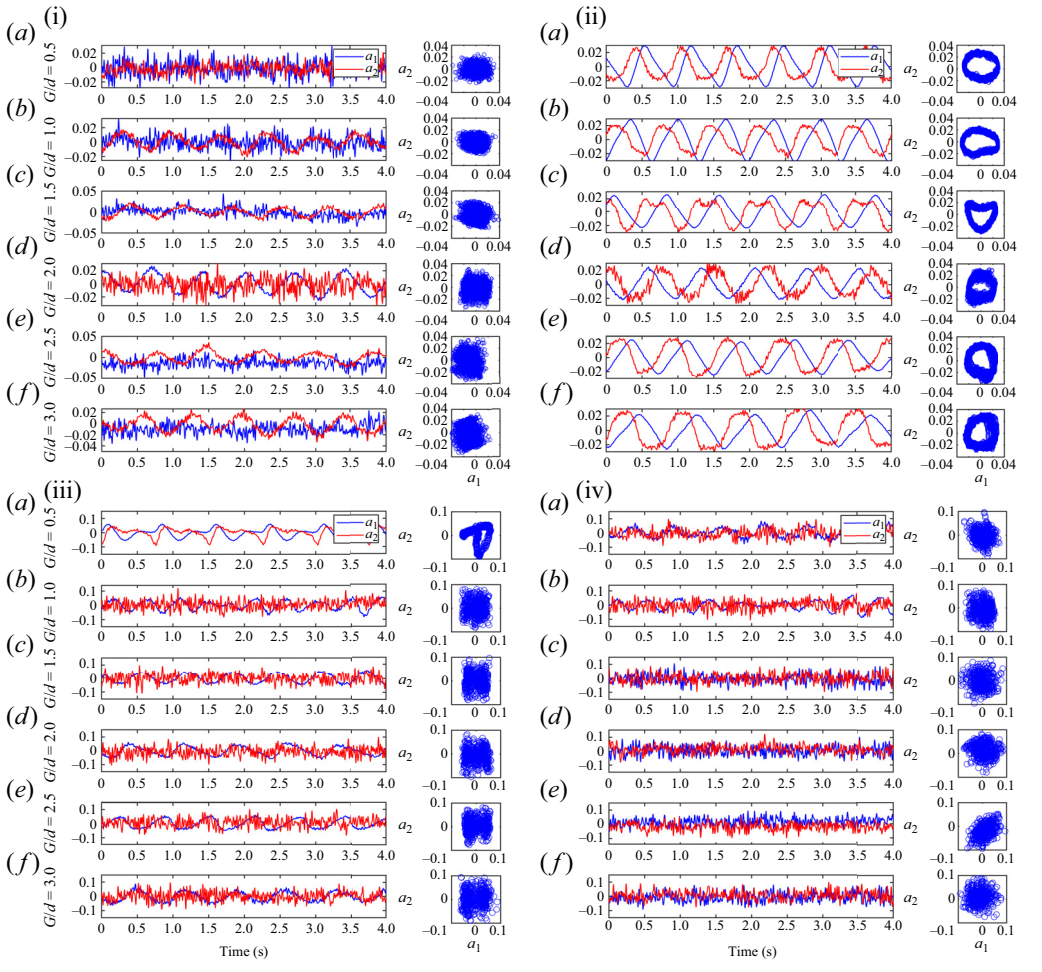

Figure 16. Coefficients versus time of the first two mode and phase diagrams at $Re = 810$. Panels show (i) $Ha = 81$, $Re/Ha = 10.0$, (ii) $Ha = 484$, $Re/Ha = 1.68$, (iii) $Ha = 888$, $Re/Ha = 0.90$ and (iv) $Ha = 1292$, $Re/Ha = 0.64$.

a strong correlation between the first two modes. The amplitude of the second-order modal coefficient is smaller than that of the first order at $G/d = 0.5$–1.5, possibly due to asymmetric shedding caused by wall effects.

Further increasing the magnetic field to $Re/Ha \approx 0.94$ in figure 16(iii), the shedding mode belongs to regime I for $G/d = 1.0$–3.0, and regime II for $G/d = 0.5$. The differences between regime I and regime II are evident. In regime I, the first-order mode still exhibits strong periodicity, while the periodicity of the second-order mode is poor. In regime II, both the first- and second-order modes have strong periodicity. The modal coefficient trajectory maintains an irregular ring shape in figure 16(iii-*a*) due to the influence of wall secondary vortices.

As the magnetic field increases to $Re/Ha \approx 0.64$ for $G/d = 1.5$–3.0, in figure 16(iv), the system reaches the 'stable state' with the energy of the first mode constituting less than 30 %. In contrast, for $G/d = 0.5$–1.0, the shedding mode corresponds to regime I with the energy of the first mode exceeding 40 %.

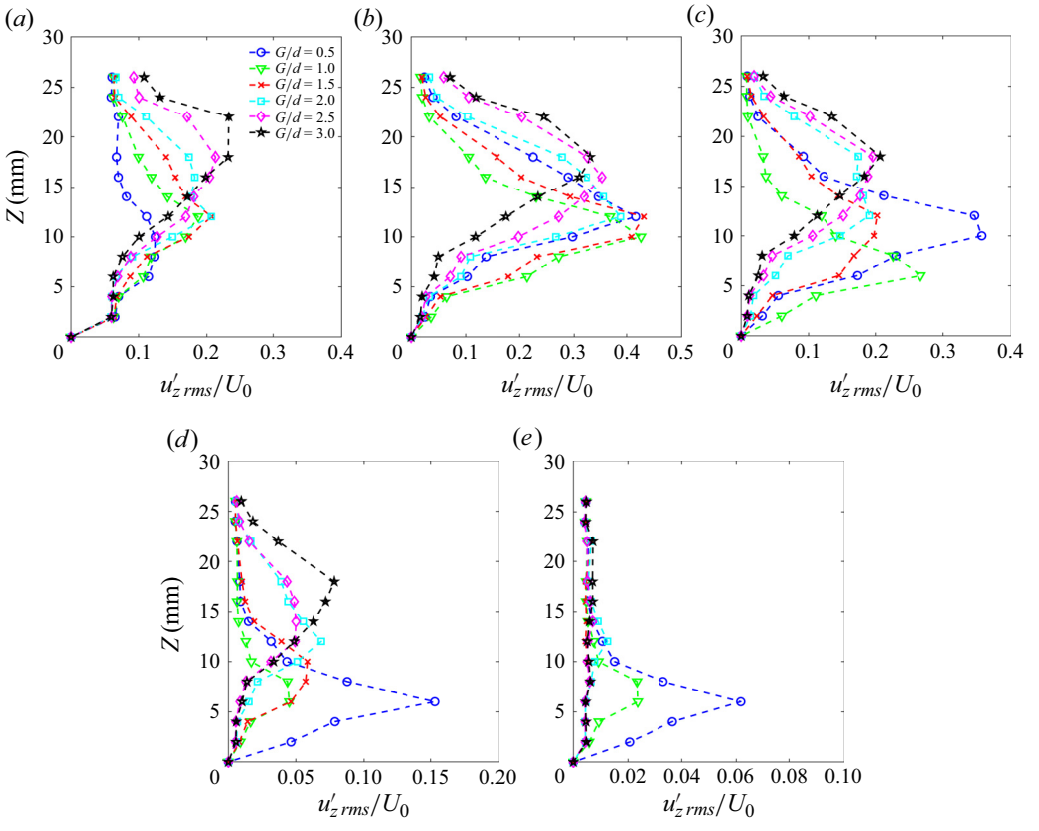

Figure 17. The r.m.s. of velocity fluctuations $(u_z')_{rms}$ for different G/d. Panels show (*a*) $Ha = 81$, $Re/Ha = 10.0$, (*b*) $Ha = 323$, $Re/Ha = 2.50$, (*c*) $Ha = 646$, $Re/Ha = 1.24$, (*d*) $Ha = 969$, $Re/Ha = 0.84$ and (*e*) $Ha = 1292$, $Re/Ha = 0.64$.

In the theory of the Kármán vortex street, the r.m.s. of vertical velocity fluctuations $(u_z')_{rms}$ divided by the inflow velocity (U_0) is a crucial dimensionless parameter that reflects the relative strength of vortices in the flow (Williamson 1996; Zdravkovich 1997). In classic Kármán vortex street, $(u_z')_{rms}/U_0$ typically ranges from 0.1 to 0.3 when Re is in the range of 40–1000. The specific value of this ratio depends on various factors, including Re, blockage ratio and turbulence.

When $Ha = 81$ (figure 17*a*), vortices in the flow break up due to 3-D effects, resulting in relatively low vortex intensity (see also figures 8*b* and 13*b*). The velocity fluctuations decrease as G/d decreases, indicating that the wall-proximity effect reduces the vortex-shedding intensity in regime III. This aligns with the conclusion in hydrodynamic flow.

When $Ha = 323$ (figure 17*b*), the flow exhibits Q2-D behaviour. The energy of small-scale 3-D vortices is transferred to the primary Q2-D vortices, leading to higher vortex intensity compared with that at $Ha = 80.8$. Furthermore, clockwise secondary vortices are generated in the Shercliff layer by K-H instability for $G/d = 0.5$–1.0. As the secondary vortices flow downstream, their energy is transported to the vortex street due to vortex pairing or merging. Consequently, as shown in figure 17(*b–e*), the vortex intensity behind a circular cylinder in proximity to a wall ($G/d = 0.5$–1.0) is higher than that behind one farther away from the wall ($G/d = 1.5$–3.0). This observation aligns with the results

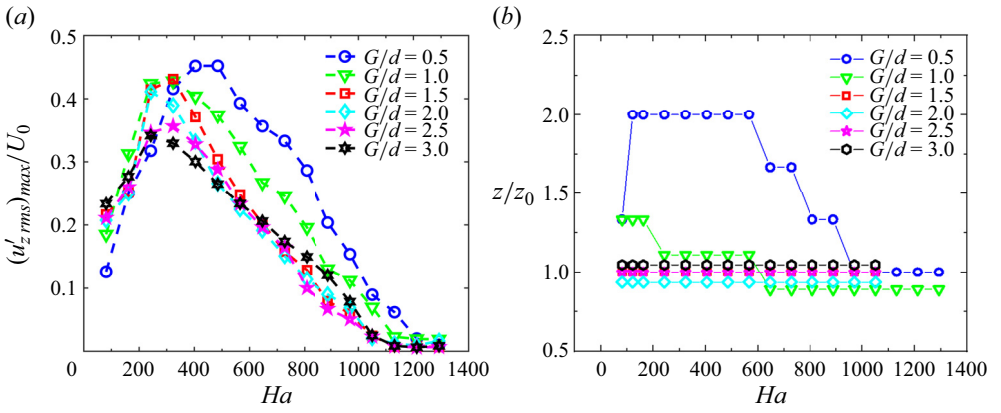

Figure 18. (*a*) Max value of non-dimensional velocity fluctuation $(u'_{z\,rms})_{max}/U_0$ against *Ha*. (*b*) Height of the point $(u'_{z\,rms})_{max}$ against *G*/*d* and *Ha*.

in hydrodynamic flow at lower gap ratios (*G*/*d*), wall-induced secondary vortices intensify the strength of the wake vortices.

As the magnetic field is increased to $Ha = 646$ (figure 17*c*), the flow remains quasi-two-dimensional. The energy of the vortices decreases with the increasing magnetic field, and $(u'_z)_{rms}/U_0$ remains above 0.1.

When the magnetic field increases to $Ha = 969$ (figure 17*d*), the vortex-shedding mode for $G/d = 1.5$–3.0 transitions to regime II, with $(u'_z)_{rms}/U_0$ falling below 0.1. Conversely, the vortex-shedding mode for $G/d = 0.5$–1.0 remains in regime I, with $(u'_z)_{rms}/U_0$ higher than 0.1.

With the magnetic field increasing to $Ha = 1292$ (figure 17*e*), the vortex-shedding mode for $G/d = 0.5$–1.0 transitions to regime I with $(u'_z)_{rms}/U_0$ less than 0.1. However, the flow transitions to the 'stable state' for $G/d = 1.5$–3.0 with $(u'_z)_{rms}/U_0$ approaching zero.

Consequently, the vortex intensity in regime II is much lower than in regime I. When the magnetic field is weak, the vortex intensity remains low due to the wall-proximity effect. When the magnetic field is strong, the wall-proximity effect promotes vortex shedding, resulting in higher vortex intensity.

4.4. *Combining influence of Ha and the wall-proximity effect*

Figure 18(*a*) illustrates the maximum values of non-dimensional velocity fluctuations in two directions against *Ha*, including data from $G/d = 0.5$–3.0. The maximum value of $(u'_{z\,rms})_{max}/U_0$ initially increases and then decreases with increasing magnetic field. The corresponding critical value of *Ha* increases with smaller *G*/*d*.

When $Ha < 484$, the maximum value of vertical velocity fluctuations for $G/d = 0.5$–1.0 is larger than that for other values of *G*/*d*. When $Ha \geq 484$, the maximum value of vertical velocity fluctuations for $G/d = 0.5$ is smaller than that for other values of *G*/*d*. Meanwhile, the decreasing tendency of $(u'_{z\,rms})_{max}$ from regime II to regime I is consistent across *G*/*d*.

Figure 18(*b*) illustrates the non-dimensional height z/z_0 of the point $(u'_{z\,rms})_{max}$ for all *G*/*d* and *Ha* values. The initial height z_0 represents the height of the cylinder core. For instance, the centre of the cylinder z_0 is positioned at $z_0 = 6$ mm for $G/d = 0.5$.

When *G*/*d* ranges from 1.5 to 3.0, the non-dimensional height z/z_0 does not change with the magnetic field, indicating that the vortex street propagates along the flow direction. However, for $G/d = 0.5$ and 1.0, the non-dimensional height z/z_0 measured at $x = 7.5d$ is

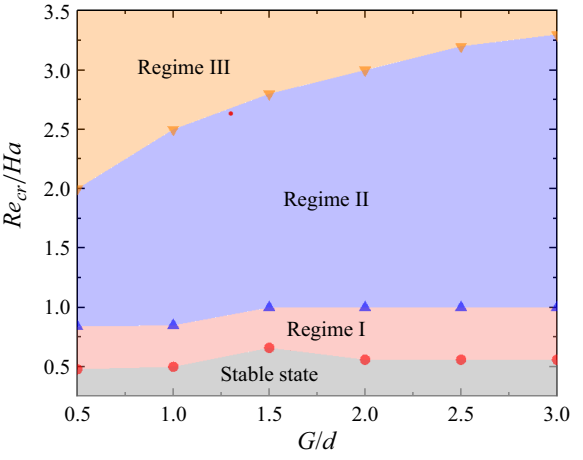

Figure 19. Critical value of (Re_{cr}/Ha) between different regimes for $G/d = 0.5$, 1.0, 1.5, 2.0, 2.5, 3.0.

higher than that at the cylinder centre. The cylinder wake rises with an upward velocity component arising from the recirculation region at the wall boundary layer, altering the trajectory of the trailing vortices.

The trajectory of the vortices aligns with the flow direction, and the height of the vortex reduces from $z = 15$ to $z = 6$ mm in a sufficiently strong magnetic field. This change in the vortex trajectory is attributed to the suppression of the recirculation region near the wall under the strengthened magnetic field.

In § 4.2, the differences in critical Re/Ha between $G/d = 2.0$ and $G/d = 0.5$ under various vortex-shedding regimes have been explained. Figure 19 illustrates the variation of critical Re/Ha for $G/d = 0.5$–3.0. For $G/d = 0.5$ and 1.0, the critical Re/Ha for the transition from regime I to the 'stable state' and from regime II to regime I are lower than those for $G/d = 1.5$–3.0. Consequently, the influence of wall effects on critical Re/Ha for transitions of 'regime II to regime I' and 'regime I to the stable state' can be neglected for $G/d \geq 1.5$. Only the critical Re/Ha for transition from regime II to regime III is all that sensitive to all values of G/d. The critical Re/Ha for the transition from regime III to regime II increases to around 3.3 as G/d rises, indicating that the wall-proximity effect causes the vortex separation point to move backward. Additionally, the wall-proximity effect promotes the transition to 3-D flow under the magnetic field. This may be related to the weak 3-D effects induced by inertial forces in the Shercliff layer.

5. Conclusion

This paper presents experiments on the effect of wall proximity on the flow around a cylinder under a strong axial magnetic field. The Kármán vortex street is observed through velocity fluctuations with a weak wall-proximity effect ($G/d = 2.0$). Additionally, the reverse Kármán street and secondary vortices are observed through velocity fluctuations under a strong wall-proximity effect ($G/d = 0.5$).

When the wall-proximity effect is weak ($G/d \geq 1.5$), three vortex-shedding modes can be distinguished: regime I ($0.56 \lesssim Re/Ha \lesssim 1.0$ for $G/d = 2.0$): shear layer oscillation states; regime II ($1.0 \lesssim Re/Ha \lesssim 3.0$ for $G/d = 2.0$): Q2-D vortex-shedding states; and regime III ($Re/Ha \gtrsim 3.0$ for $G/d = 2.0$): transition of magnetohydrodynamic to hydrodynamic Kármán street. In regime I, the vortex-shedding mechanism, caused by the K-H instability

of the shear layer stretched by the magnetic field, differs from the traditional Kármán vortex street. When Re ranges from 360 to 810, the vortex-shedding frequency increases with Ha in regime I, whereas it decreases with increasing Ha in regime II. In regime III, the vortex-shedding frequency exhibits a 'jump' for $Re \sim 720$–810. Furthermore, the energy of the vortices in regime II gradually diminishes with the intensification of the magnetic field, while in regime I, it precipitously drops as the magnetic field strengthens until the K-H instability in the shear layer behind the cylinder is completely suppressed by the magnetic field, preventing vortex shedding altogether.

With a strong wall-proximity effect ($G/d \leq 1.0$), the vortex-shedding modes remain three in number, but the critical Re_{cr}/Ha between these modes varies. The energy of secondary vortices is transferred to the Kármán vortex street, enhancing vortex intensity due to the wall-proximity effect. A higher magnetic field is required to completely suppress the wake with a lower critical $Re_{cr}/Ha = 0.48$ from regime I ($0.48 \lesssim Re/Ha \lesssim 0.84$ for $G/d = 0.5$) to a stable state. In other words, the instability of Shercliff layer promotes vortex shedding in MHD flow around a cylinder, contrary to the conclusion that the wall shear layer suppresses vortex shedding in hydrodynamics. Moreover, the Shercliff layer has weak 3-D characteristics, requiring a lower Re_{cr}/Ha ($Re_{cr}/Ha = 2.0$ for $G/d = 0.5$) to transition the flow from regime III ($Re/Ha \gtrsim 2.0$ for $G/d = 0.5$) to regime II ($0.84 \lesssim Re/Ha \lesssim 2.0$ for $G/d = 0.5$). When the magnetic field is weak ($Re/Ha \gtrsim 0.84$), the secondary vortices shed from the bottom wall, leading to an obliquely propagating wake street. When the magnetic field increases ($0.48 \lesssim Re/Ha \lesssim 0.84$), the secondary vortices are suppressed, resulting in the wake aligning along the streamwise direction.

Further analysis using the POD method revealed distinctions among the three regimes of vortex shedding. With the magnetic field increasing, the flow transitions from regime III to regime II with the first mode energy increasing up to 90 %. However, the energy proportion of the first mode drops down to 50 % when the flow transitions from regime II to regime I.

Vortex streets near the wall promote the growth of disturbances within the boundary layer, indicating the influence of different gap ratios on the instability conditions of various boundary layers. Nevertheless, the restriction of the number of electrical potential probes precludes this study from establishing the critical condition for the K-H instability of the Shercliff layer as identified by Chatterjee & Gupta (2015). Additionally, the location of the probes was too far from the cylinder to observe the secondary vortex shedding from the recirculation region in the Shercliff layer. Nevertheless, understanding the dynamic characteristics of MHD flow around an obstacle, as discussed in this paper, is beneficial for studying heat transfer enhancement mechanisms in the design of nuclear fusion reactors. Specifically, the results provide insights into how magnetic field and wall-proximity effects influence the vortex dynamics. In the future, additional research could experimentally measure the direct impact of this dynamics on heat transfer.

Funding. The authors gratefully acknowledge support from the National Natural Science Foundation of China (NSFC) under grant nos. 52176089 and U23B20110.

Declaration of interests. The authors report no conflict of interest.

Author ORCIDs.
Ze-Dong Wang https://orcid.org/0009-0000-8826-9941;
Ming-Jiu Ni https://orcid.org/0000-0003-3699-8370;
Nian-Mei Zhang https://orcid.org/0000-0001-5400-9607.

References

Abdou, M., Morley, N.B., Smolentsev, S., Ying, A., Malang, S., Rowcliffe, A. & Ulrickson, M. 2015 Blanket/first wall challenges and required R&D on the pathway to DEMO. *Fusion Engng Des.* **100**, 2–43.

Andreev, O. & Kolesnikov, Y.B. 1998 Experimental investigation of a flow around a conducting cylinder in an axial homogeneous magnetic field. *Magnetohydrodynamics* **34** (4), 286–293.

Bearman, P.W. & Zdravkovich, M.M. 1978 Flow around a circular cylinder near a plane boundary. *J. Fluid Mech.* **89** (1), 33–47.

Belyaev, I., Sardov, P., Melnikov, I. & Frick, P. 2021 Limits of strong magneto-convective fluctuations in liquid metal flow in a heated vertical pipe affected by a transverse magnetic field. *Intl J. Therm. Sci.* **161**, 106773.

Belyaev, I.A., Mironov, I.S., Luchinkin, N.A., Listratov, Y.I., Kolesnikov, Y.B., Kransov, D., Zikanov, O. & Molokov, S. 2022 Experimental study of submerged liquid metal jet in a rectangular duct in a transverse magnetic field. *J. Fluid Mech.* **953**, A10.

Bühler, L., Mistrangelo, C. & Brinkmann, H.-J. 2020 Experimental investigation of liquid metal MHD flow entering a flow channel insert. *Fusion Engng Des.* **154**, 111484.

Burr, U., Barleon, L., Müller, U. & Tsinober, A. 2000 Turbulent transport of momentum and heat in magnetohydrodynamic rectangular duct flow with strong sidewall jets. *J. Fluid Mech.* **406**, 247–279.

Cassells, O.G.W., Hussam, W.K. & Sheard, G.J. 2016 Heat transfer enhancement using rectangular vortex promoters in confined quasi-two-dimensional magnetohydrodynamic flows. *Intl J. Heat Mass Transfer* **93**, 186–199.

Cassells, O.G.W., Vo, T., Pothérat, A. & Sheard, G.J. 2019 From three-dimensional to quasi-two-dimensional: transient growth in magnetohydrodynamic duct flows. *J. Fluid Mech.* **861**, 382–406.

Chatterjee, D. & Gupta, S.K. 2015 MHD flow and heat transfer behind a square cylinder in a duct under strong axial magnetic field. *Intl J. Heat Mass Transfer* **88**, 1–13.

Davidson, P.A. 1997 The role of angular momentum in the magnetic damping of turbulence. *J. Fluid Mech.* **336**, 123–150.

Dipankar, A. & Sengupta, T.K. 2005 Flow past a circular cylinder in the vicinity of a plane wall. *J. Fluids Struct.* **20** (3), 403–423.

Dousset, V. & Pothérat, A. 2008 Numerical simulations of a cylinder wake under a strong axial magnetic field. *Phys. Fluids* **20** (1), 017104.

Dousset, V. & Pothérat, A. 2012 Characterization of the flow past a truncated square cylinder in a duct under a spanwise magnetic field. *J. Fluid Mech.* **691**, 341–367.

Eckert, S., Cramer, A. & Gerbeth, G. 2007 Velocity measurement techniques for liquid metal flows. In *Magnetohydrodynamics*. Fluid Mechanics and its Applications, vol. 3, pp. 275–294. Springer.

Frank, M., Barleon, L. & Müller, U. 2001 Visual analysis of two-dimensional magnetohydrodynamics. *Phys. Fluids* **13** (8), 2287–2295.

Hamid, A.H.A., Hussam, W.K., Pothérat, A. & Sheard, G.J. 2015 Spatial evolution of a quasi-two-dimensional kármán vortex street subjected to a strong uniform magnetic field. *Phys. Fluids* **27** (5), 053602.

He, G.-S. & Wang, J.-J. 2015 Flat plate boundary layer transition induced by a controlled near-wall circular cylinder wake. *Phys. Fluids* **27** (2), 024106.

He, G.-S., Wang, J.-J., Pan, C., Feng, L.-H., Gao, Q. & Rinoshika, A. 2017 Vortex dynamics for flow over a circular cylinder in proximity to a wall. *J. Fluid Mech.* **812**, 698–720.

Hunt, J.C.R. & Ludford, G.S.S. 1968 Three-dimensional MHD duct flows with strong transverse magnetic fields. Part 1. Obstacles in a constant area channel. *J. Fluid Mech.* **33** (04), 693.

Hussam, W.K., Hamid, A.H.A., Ng, Z.Y. & Sheard, G.J. 2018 Effect of vortex promoter shape on heat transfer in MHD duct flow with axial magnetic field. *Intl J. Therm. Sci.* **134**, 453–464.

Hussam, W.K. & Sheard, G.J. 2013 Heat transfer in a high hartmann number MHD duct flow with a circular cylinder placed near the heated side-wall. *Intl J. Heat Mass Transfer* **67**, 944–954.

Hussam, W.K., Thompson, M.C. & Sheard, G.J. 2011 Dynamics and heat transfer in a quasi-two-dimensional MHD flow past a circular cylinder in a duct at high Hartmann number. *Intl J. Heat Mass Transfer* **54** (5–6), 1091–1100.

Hussam, W.K., Thompson, M.C. & Sheard, G.J. 2012 Optimal transient disturbances behind a circular cylinder in a quasi-two-dimensional magnetohydrodynamic duct flow. *Phys. Fluids* **24** (2), 024105.

Jiang, H. & Cheng, L. 2017 Strouhal–Reynolds number relationship for flow past a circular cylinder. *J. Fluid Mech.* **832**, 170–188.

KANARIS, N., ALBETS, X., GRIGORIADIS, D. & KASSINOS, S. 2013 Three-dimensional numerical simulations of magnetohydrodynamic flow around a confined circular cylinder under low, moderate, and strong magnetic fields. *Phys. Fluids* **25** (7), 074102.

KIYA, M., TAMURA, H. & ARIE, M. 1980 Vortex shedding from a circular cylinder in moderate-Reynolds-number shear flow. *J. Fluid Mech.* **141** (4), 721–735.

KLEIN, R., POTHÉRAT, A. & ALFERENOK, A. 2009 Experiment on a confined electrically driven vortex pair. *Phys. Rev.* E **79** (1), 016304.

KOLESNIKOV, Y.B. & TSINOBER, A.B. 1976 Experimental investigation of two-dimensional turbulence behind a grid. *Fluid Dyn.* **9** (4), 621–624.

KUSUMI, K., KUNUGI, T., YOKOMINE, T., KAWARA, Z., WU, Y., SAGARA, A. & TANAKA, T. 2019 Thermal mixing enhancement of liquid metal film-flow by various obstacles under vertical magnetic field. *Fusion Engng Des.* **146**, 2158–2162.

MESSADEK, K. & MOREAU, R. 2002 An experimental investigation of MHD quasi-two-dimensional turbulent shear flows. *J. Fluid Mech.* **456**, 137–159.

MISTRANGELO, C. & BÜHLER, L. 2018 Determination of multichannel MHD velocity profiles from wall-potential measurements and numerical simulations. *Fusion Engng Des.* **130**, 137–141.

MISTRANGELO, C., BÜHLER, L., ALBERGHI, C., BASSINI, S., CANDIDO, L., COURTESSOLE, C., TASSONE, A., URGORRI, F.R. & ZIKANOV, O. 2021 MHD R&D activities for liquid metal blankets. *Energies* **14** (20), 6640.

MOREAU, R. 1990 *Magnetohydrodynamics*. Fluid Mechanics and its Applicaitons, vol. 3. Springer.

MORLEY, N.B., BURRIS, J., CADWALLADER, L.C. & NORNBERG, M.D. 2008 Gainsn usage in the research laboratory. *Rev. Sci. Instrum.* **79** (5), 056107.

MÜCK, B., GÜNTHER, C., MÜLLER, U. & BÜHLER, L. 2000 Three-dimensional MHD flows in rectangular ducts with internal obstacles. *J. Fluid Mech.* **418**, 265–295.

MÜLLER, U. & BÜHLER, L. 2001 *Magnetofluiddynamics in Channels and Containers*. Springer.

PAN, J.-H., ZHANG, N.-M. & NI, M.-J. 2019 Wake structure of laminar flow past a sphere under the influence of a transverse magnetic field. *J. Fluid Mech.* **873**, 151–173.

POTHÉRAT, A. 2007 Quasi-two-dimensional perturbations in duct flows under transverse magnetic field. *Phys. Fluids* **19** (7), 074104.

POTHÉRAT, A. & KLEIN, R. 2014 Why, how and when MHD turbulence at low becomes three-dimensional. *J. Fluid Mech.* **761**, 168–205.

RHOADS, J.R., EDLUND, E.M. & JI, H. 2014 Effects of magnetic field on the turbulent wake of a cylinder in free-surface magnetohydrodynamic channel flow. *J. Fluid Mech.* **742**, 446–465.

SMOLENTSEV, S. 2023 Modeling of transport processes in liquid-metal fusion blankets: past, present, and future. *Fusion Sci. Technol.* **79** (3), 251–273.

SMOLENTSEV, S., MORLEY, N.B., ABDOU, M.A. & MALANG, S. 2015 Dual-coolant lead–lithium (DCLL) blanket status and R&D needs. *Fusion Engng Des.* **100**, 44–54.

SOMMERIA, J. & MOREAU, R. 1982 Why, how, and when, MHD turbulence becomes two-dimensional. *J. Fluid Mech.* **118** (1), 507.

SREENIVASAN, B. & ALBOUSSIÈRE, T. 2002 Experimental study of a vortex in a magnetic field. *J. Fluid Mech.* **464**, 287–309.

THOMPSON, M.C., LEWEKE, T. & HOURIGAN, K. 2021 Bluff bodies and wake–wall interactions. *Annu. Rev. Fluid Mech.* **53** (1), 347–376.

WILLIAMSON, C.H.K. 1996 Vortex dynamics in the cylinder wake. *Annu. Rev. Fluid Mech.* **28** (1), 477–539.

ZDRAVKOVICH, M.M. 1997 *Flow Around Circular Cylinder Vol 1: Fundamentals*. Oxford University Press.

ZHANG, X.-F., YANG, J.-C., NI, M.-J., ZHANG, N.-M. & YU, X.-G. 2023 Numerical simulations of flow around dual tandem circular cylinders under a strong axial magnetic field. *Phys. Fluids* **35** (2), 023604.

ZHOU, J., QIU, X., LI, J. & LIU, Y. 2021 The gap ratio effect on evolution behind a cylinder placed near a wall. *Phys. Fluids* **33** (3), 037112.

ZOVATTO, L. & PEDRIZZETTI, G. 2001 Flow about a circular cylinder between parallel walls. *J. Fluid Mech.* **440**, 1–25.